UNIVERSITY OF GRONINGEN, GRONINGEN

MASTER THESIS

FACULTY OF SCIENCE AND ENGINEERING

On-surface polymerization of 6,12-dibromochrysene on Ag(111)

First examiner:
Prof. Dr. M. A. Stöhr
Second examiner:
Prof. Dr. T. Banerjee
Daily supervisor:
R. S. K. Houtsma

Author:
J.A.M. van Zuilen
S3133516

April 2022

Abstract

Graphene nanoribbons (GNRs) combine the unique electronic properties of graphene with the opening of a bandgap. This makes GNRs an interesting candidate for replacing silicon in electronic devices. GNRs can be synthesized with atomic precision using on-surface synthesis techniques. This atomic precision is necessary to further study the electronic properties of GNRs. Previously, chevron-like GNRs were synthesized on Au(111) from the prochiral molecular precursor 6,12-dibromochrysene (DBCh).[1] In the same study, it was found that no GNRs are formed on Cu(111) using the same procedure.[1] Moreover, a similar study found that no GNRs can be synthesized on Ag(110) from this molecular precursor.[2] This work aims to broaden the understanding of the influence of the substrate by studying the on-surface polymerization of DBCh on Ag(111) in ultra-high vacuum using scanning tunneling microsopy. Deposition of this molecule at room temperature leads to the formation of four different self-assemblies. These self-assemblies consist of both fully debrominated DBCh molecules and partially debrominated molecules. Deposition at elevated temperatures leads to the formation of (networks of) heterochiral chains. Specifically, deposition at a 150°C leads to the formation of heterochiral chains in which the left- and right-handed enantiomers alternate. Further annealing breaks these chains and leads to the formation of disordered clumps of molecules. It is concluded that the formed networks cannot be transformed to GNRs because of the strong metal-coordination with a silver adatom rather than due to the chiral-selectivity.

Contents

1   Introduction

In 1969, the Apollo Guidance Computers (AGC) of the Apollo 11 assisted Neil Armstrong and his crew on their mission to the moon. The AGC consisted of 2048 integrated circuits (ICs) with only several tens of thousand of transistors.[3, 4] The AGC had the dimensions of a large backpack and weighed over 30 kilograms.[5] In comparison, the Iphone XS, produced in 2018, has a processor containing 6.9 billion transistors and fits in your pocket.[6, 7] This immense growth in the number of transistors in ICs was predicted in 1965 by Gordon Moore, the co-founder of Intel. Moore predicted with his emperical law that the number of transistors in an IC will double about every two years.[8]

Currently, the most powerful ICs are produced using industrial state of the art photolithography with a wavelength of 13.5nm, leading to features as small as 5 to 7nm. Photolithography is a top-down approach which uses extreme ultraviolet light to produce silicon-based electronics. Unfortunately, stochastic effects in photolithography limit the miniaturization of transistors in silicon-based electronics. Thus, in order to cramp more transistors in devices that fit in your pocket, other ways of producing ICs have to be explored. One way of doing this is by switching to a bottom-up approach. In a bottom-up approach atoms and molecules are used as building blocks to create nano-architectures, see for example Ref. [9]

Another way of producing more computing power is by finding an alternative for silicon-based electronics. Since the first mechanical exfoliation of graphene from graphite in 2004 [10], graphene has been a candidate material for replacing silicon in electronics. Graphene, the two-dimensional allotrope of carbon, has a high conductivity [11] and is subject to the field effect [10]. Graphene is a semi-metal, meaning that it has no bandgap. In order for graphene to be realized as the successor of silicon, a bandgap has to opened.

A bandgap can be opened by applying strain to the graphene, by doping or by constraining the graphene layer in one direction to form a graphene nanoribbon. The last option, synthesizing a graphene nanoribbon, will be explored in this thesis. Due to quantum confinement of the electrons in the ribbon a bandgap opens.[12] The size of the bandgap can be tuned by tuning the width of the ribbon or by changing the edge termination of the ribbon.[13, 14] Using a bottom-up approach, specifically on-surface synthesis, these graphene nanoribbons can be produced with atomic precision.[15] This allows for application in electronics [11, 16, 17], photonics [18] and energy storage [19].

In the on-surface synthesis of graphene nanoribbons, a molecular precursor is deposited onto a metallic substrate. This sample is then annealed which leads to the formation of polymers. The formed polymers can be transformed into graphene nanoribbons upon further annealing. Using this on-surface synthesis method, ribbons with armchair [20–23], zigzag [24, 25], chevron [1, 15] and chiral [20] edge termination have been synthesized. Using a scanning tunneling microscope, these ribbons can be studied in high resolution in real space.

In this thesis, the on-surface polymerization of 6,12-dibromochrysene on Ag(111) was studied. Previous work by Pham *et al.*, showed that chevron-type graphene nanoribbons can be synthesized on an Au(111) substrate from this precursor molecule.[1] However, the same work showed that no graphene nanoribbons were produced on a Cu(111) substrate. Moreover, recent work in this group showed that no graphene nanoribbons can be synthesized on an Ag(110) substrate from this precursor.[2] By studying the same precursor molecule on Ag(111) the mechanisms behind its on-surface synthesis and molecular self-assembly can be better understood. The on-surface polymerization will be studied with an ultra-high vacuum low-temperature scanning tunneling microscope. A brief introduction to this technique is given in Section 3. The theoretical background on graphene, graphene nanoribbons and molecular self-assembly is given in Section 2. After the theory and experimental methods are described, the results will be given and discussed in Section 4. A general discussion spanning the different experiments in this thesis will be given in Section 5, after which it will be concluded in Section 6.

2   Theoretical background

2.1   Graphene

Graphene is a two-dimensional allotrope of carbon, where the carbon atoms are arranged in a honeycomb lattice as depicted in Figure 1a. It was experimentally obtained for the first time from graphite by Novoselov *et al.* in 2004 [10] and has been extensively studied since.[26] It is a semi-metal, meaning that graphene has no bandgap. Yet, graphene is expected to be a candidate material for replacing silicon in electronics because of its high conductivity [11], as long as a bandgap can be opened. Its structure is not made up of a Bravais lattice (not every atom has identical surrounding) but can be seen as two triangular sublattices. The lattice vectors are given by:

$$\mathbf{a_1} = \frac{a}{2}(3, \sqrt{3}), \qquad \mathbf{a_2} = \frac{a}{2}(3, -\sqrt{3}) \qquad (1)$$
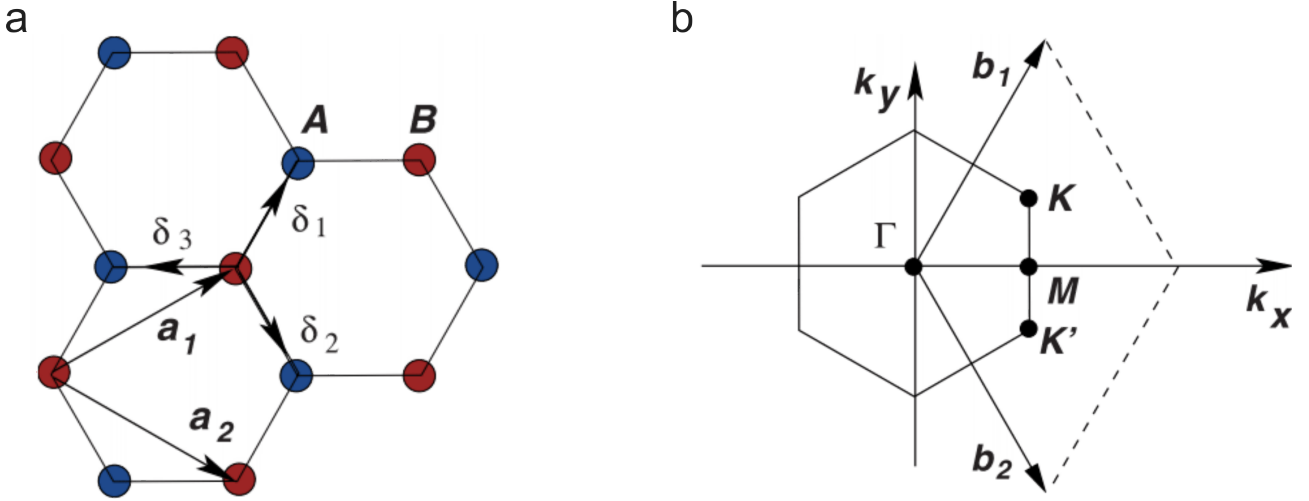
Figure 1: *a) The lattice structure of graphene, which consists of two sublattices A and B, colored blue and red respectively. The unit cell vectors are depicted as $\mathbf{a_1}$ and $\mathbf{a_2}$ and the nearest neighbour vectors are depicted as δ_1, δ_2 and δ_3. b) The Brillioun zone of graphene, in which the K and K' points can be seen. Adapted from Ref. [27]*

where $a \approx 1.42$ Å is the distance between carbon atoms.[27] The reciprocal lattice vectors can be found using $\mathbf{a}_i \cdot \mathbf{b}_j = 2\pi\delta_{ij}$ [28], and are:

$$\mathbf{b_1} = \frac{2\pi}{3a}(1, \sqrt{3}), \qquad \mathbf{b_2} = \frac{2\pi}{3a}(1, -\sqrt{3}) \tag{2}$$

The sp^2 hybridization of the orbitals leads to the structure seen in Figure 1a, where there is a σ-bond between carbon atoms. These σ-bonds lead to the excellent structural properties of graphene. The p_z orbitals, which do not take part in the sp^2 hybridization, are perpendicular to the planar structure. These orbitals bind covalently with neighbouring carbon atoms, forming a π-band.

To understand the unique electronic properties of graphene, we must find the energy dispersion relation. This is done using the tight-binding Hamiltonian with nearest-neighbour hopping constant t and next-nearest-neighbour hopping constant t'. The Hamiltonian is given by:

$$H = -t \sum_{\langle i,j \rangle, \sigma} \left(a_{\sigma,i}^\dagger b_{\sigma,j} + h.c. \right) - t' \sum_{\langle\langle i,j \rangle\rangle, \sigma} \left(a_{\sigma,i}^\dagger a_{\sigma,j} + b_{\sigma,i}^\dagger b_{\sigma,j} + h.c. \right) \tag{3}$$

where $a_{\sigma,i}$ ($a_{\sigma,i}^\dagger$) annihilates (creates) an electron with spin $\sigma = \uparrow, \downarrow$. Hopping between two nearest neighbours is described by t ($t \approx 2.8eV$) and hopping to next-nearest neighbours is described by t' ($0.02t \lesssim t' \lesssim 0.2t$)[1]. Using these values for t and t', the energy bands are given by:

$$E_\pm(\mathbf{k}) = \pm t\sqrt{3 + f(\mathbf{k})} - t'f(\mathbf{k}), \tag{4}$$

where

$$f(\mathbf{k}) = 2\cos\left(\sqrt{3}k_y a\right) + 4\cos\left(\frac{\sqrt{3}}{2}k_y a\right)\cos\left(\frac{3}{2}k_x a\right), \tag{5}$$

in which the plus depicts the upper energy band and the minus depicts the lower energy band. A plot of the energy bands is depicted in Figure 2.

At the corners of the Brillioun zone, depicted in Figure 1b, we see the K and K' points. These points are also called the Dirac points of graphene. The positions of the Dirac points in k-space are given by:

$$\mathbf{K} = \left(\frac{2\pi}{3a}, \frac{2\pi}{3\sqrt{3}a}\right), \qquad \mathbf{K}' = \left(\frac{2\pi}{3a}, -\frac{2\pi}{3\sqrt{3}a}\right) \tag{6}$$

By expanding Equation 4 around the K points using $\mathbf{k} = \mathbf{K} + \mathbf{q}$ and $|\mathbf{q}| \ll |\mathbf{K}|$, the energy dispersion close to the Dirac points is found to be:

$$E_\pm(\mathbf{q}) \approx \pm v_F|\mathbf{q}| + \mathcal{O}((q/K)^2), \tag{7}$$

where $\mathbf{q}$ is the momentum measured relative to the K points and v_F is the Fermi velocity ($v_F = 3ta/2$). Neglecting the higher order terms and setting the next-nearest neighbour hopping constant to zero, we are left

---

[1]The value of t' is not exactly known, but has been approximated using *ab initio* calculations. The value depends on the tight-binding parameterization.[27]
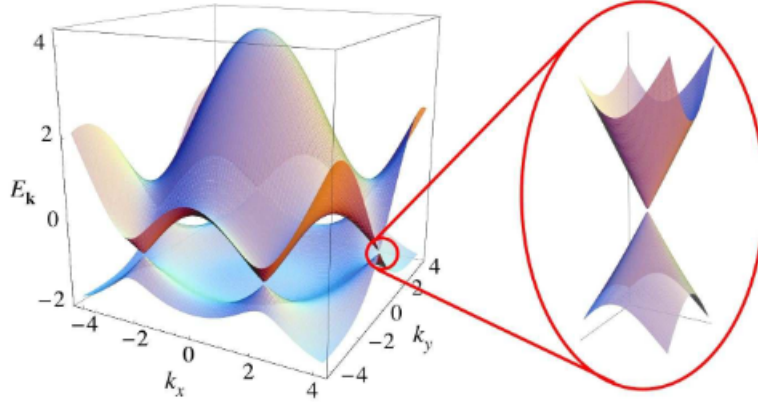
Figure 2: *The energy bands of graphene in units of t, with t = 2.7eV and t′ = 0.2t. The zoom-in depicts the band structure around the Dirac points, from which the linear relationship in the energy dispersion can be clearly seen. Adapted from Ref. [27]*
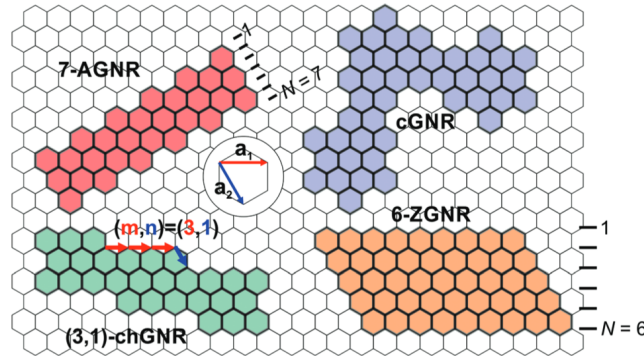

Figure 3: *Schematic depicting four classes of GNRs and their classification. AGNRs are identified by the number of dimer lines, ZGNRs are identified by the amount of zigzag lines, chGNRs are identified by their width and edge orientation and there is currently no agreement on the classification for cGNRs. Adapted from Ref. [33]*

with a linear dispersion relationship around the Dirac points. This greatly differs from the parabolic dispersion seen in metals. This important result was first obtained by Wallace in 1947 [29] and is the reason for some of the fascinating electronic properties of graphene. The linear energy dispersion relation, shown in Equation 7, shows that graphene has no bandgap. The bandgap can be opened in several distinct ways, for example by applying strain to the graphene or by constraining the graphene layer in one direction to form a graphene nanoribbon.[11]

2.1.1 Graphene nanoribbons

By fabricating a ribbon of graphene that is only a few nanometers wide, called a graphene nanoribbon (GNR), a bandgap can open up due to quantum confinement of the electrons.[12] The size of the bandgap can be tuned by changing the width of the GNR, see for example Refs. [13, 30–32]

GNRs come in four different classes: armchair (AGNRs), zigzag (ZGNRs), chiral (chGNRs) and chevron (cGNRs), which are shown in Figure 3.[33] In order to identify the width of AGNRs, the number of dimer lines is counted, e.g. Figure 3 depicts a 7-AGNR. In the case of ZGNRs, the width is expressed as the number of zigzag lines, e.g. Figure 3 depicts a 6-ZGNR. chGNRs are identified by their width and edge orientation. cGNRs consist of a combination of armchair and zigzag edges, and there is no agreed upon classification.

2.1.1.1 Energy dispersion relation of GNRs

The energy dispersion relation of AGNRs and ZGNRs can be approximated using the zone-folding approach and the tight-binding approximation.[12] In the zone-folding approach the energy band structure (Figure 4) of graphene is projected onto an armchair or zigzag edge. The resulting band structures for AGNRs and ZGNRs are depicted in Figures 4b and 4d, respectively. Nakada *et al.* showed that AGNRs with a width of $3p + 2$ (with p an integer) are metallic, whereas AGNRs with any other width have a bandgap.[12] ZGNRs are expected to
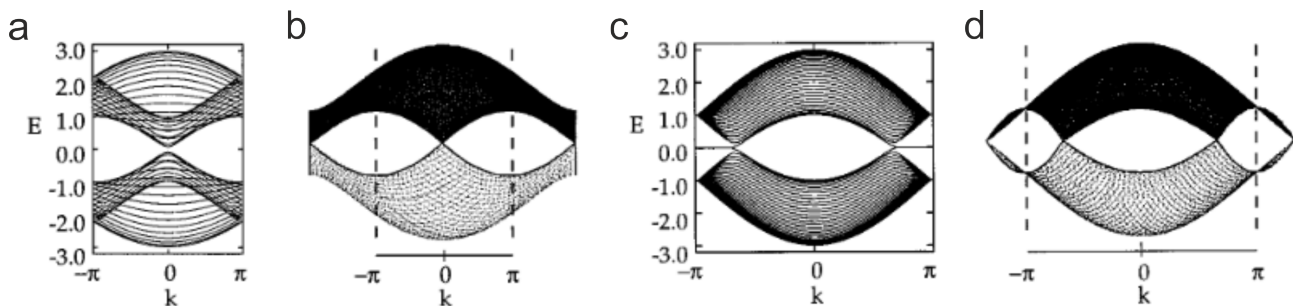
Figure 4: *a) Calculated band structure of a N = 30 AGNR. b) Projected band structure of graphene onto an armchair axis. c) Calculated band structure of a ZGNR. d) Projected band structure of graphene onto a zigzag axis. In b) and d) the dashed lines indicate the boundaries of the Brillioun zone. Adapted from Ref. [12]*

be metallic for any width. However, when calculating the energy dispersion of ZGNRs using the tight-binding approach a flatband occurred (Figure 4c), which was not found in the zone-folding approach. This flatband structure is theorised to originate from edge states at the zigzag edge, which are not found in AGNRs.

A more complete picture of the energy dispersion relation can be found using density functional theory (DFT) calculations. Using DFT, Son *et al.* showed that for every width of an AGNR a bandgap opens.[13] According to their work, AGNRs can be divided into three classes depending on the width of the ribbon: $3p+1$, $3p$ and $3p+2$, where p is an integer. The size of the bandgap Δ depends on the class, where $\Delta_{3p+1} > \Delta_{3p} > \Delta_{3p+2}(\neq 0)^2$, see Figure 5. This size hierarchy shows that a decrease in width does not always lead to an increase in bandgap, as was predicted by tight-binding calculations. The bandgap of $(3p + 2)$-AGNRs opens because of edge effects. The carbon atoms at the edge of the AGNRs are passivated by hydrogen atoms, which leads to a difference in bond length between carbon atoms at the edge and those in the middle of the AGNR. The hopping constant thus differs, leading to the opening of the bandgap in $(3p + 2)$-AGNRs and a reduction of the bandgap of $(3p + 1)$-AGNRs. Furthermore, in contrast to the zone-folding approach, using DFT calculations it was shown that ZGNRs are semiconducting as well. The flatband at the Fermi-level originating from the edge states has a high density of states (DOS) according to tight-binding calculations. This leads to to spin-polarization through electron-electron interactions and with that an opening of the bandgap.[33]

2.1.1.2 Atomically precise GNRs

GNRs can be fabricated with atomic precision using an on-surface bottom-up approach, as was first shown by Cai *et al.* in 2010.[15] Most importantly, on-surface synthesis allows for synthesizing the GNRs with atomic precision. Atomic precision is of the utmost importance, as a small alteration in the width or edge termination can already impact the electronic and transport properties of a GNR.[33] Another advantage of an on-surface bottom-up approach is that it reduces the $\pi - \pi$ stacking between planar nanographenes, making the GNRs soluble in commonly used solvents.[34] The reduced stacking also reduces the sublimation temperature so that it is lower than the decomposition temperature, making it possible to bring these structures to another substrate or device.[34]

In short, the synthesizing process generally consists of three steps. In the first step, precursor molecules are evaporated on a single crystal of choice. The precursor is a halogenated aromatic molecule, like 6,12-dibromochrysene (see Section 2.4). In the following step the precursor molecules are dehalogenated by thermal annealing of the sample. The positions of the halogen atoms define the positions at which the covalent bonds in the next step form. This means that the final structure (the GNR) can be predicted from the precursor molecule. The dehalogenated molecules form either metal-organic coordination structures with native substrate adatoms or polymers based on an Ullmann-type reaction. Finally, the polymer is converted into a GNR through cyclodehydrogenation upon annealing at a temperature larger than the one used for polymer formation. This results in a GNR with an atomically precise width and edge structure. A more detailed description of every step and its processes is given in the following sections.

2.2 Molecules on surfaces

2.2.1 Molecular self-assembly

Molecular self-assembly was defined as the "*spontaneous assembly of molecules into structured, stable, non-covalently joined aggregates under equilibruim*" by Whitesides *et al.* in 1991.[35] Molecular self-assembly has shown to be a promising strategy for the synthesis of structures, paving the road to molecular electronics.

---

^{2}Rather than $\Delta_{3p} \gtrsim \Delta_{3p+1} > \Delta 3p + 2(= 0)$ as shown by tight-binding calculations.
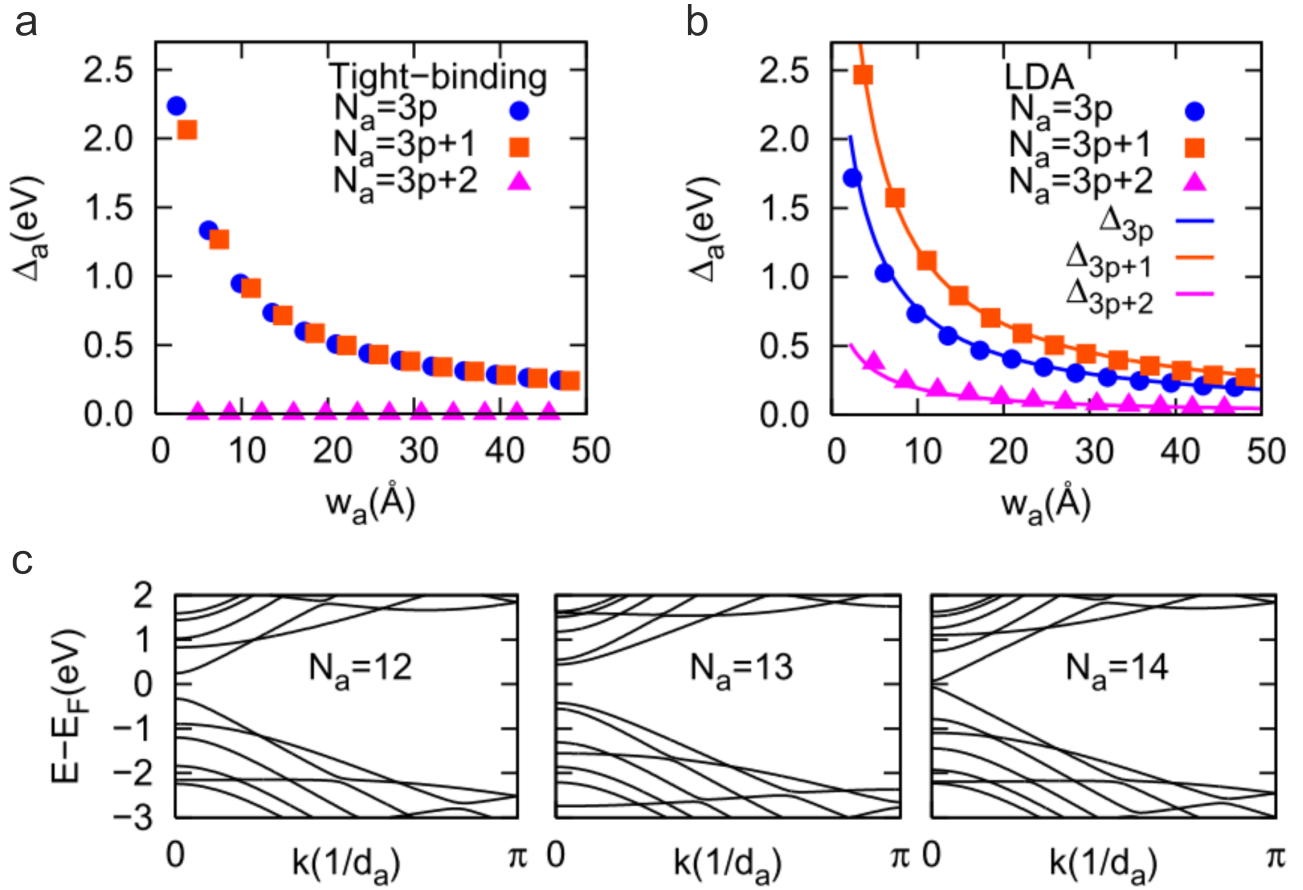
Figure 5: *a) The variation of the bandgap of AGNRs as a function of width (w_a) obtained using tight-binding calculations with $t = 2.70$ eV. b) The variation of the bandgap of AGNRs as a function of width (w_a) obtained using DFT calculations. The solid line depicts the solution of the Hamiltonian, see [13] for more detail. c) DFT calculations of the band structures of AGNRs of width 12, 13 and 14, respectively. Adapted from Ref. [13]*
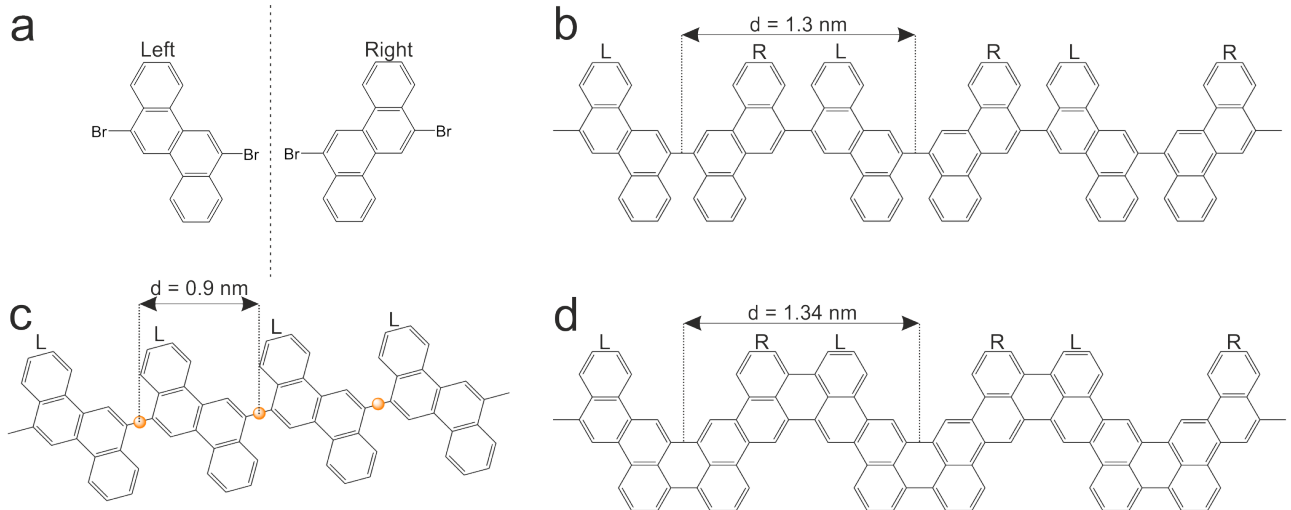
Figure 6: *a) The left- and right-handed enantiomers of DBCh. b) The polymer formed from DBCh on Au(111) upon thermal annealing. c) The metal-organic coordinated polymer formed upon deposition of DBCh on Cu(111) at room temperature. The orange circles indicate Cu adatoms. d) chGNR formed upon annealing the polymer formed on Au(111). The difference between the polymer and the chGNR is the extra C-C bond where left- and right-handed enantiomers coordinate.*

Table 1: *Classification of intermolecular interactions in molecular self-assembly. Based on Ref. [37]*

	Energy range	Distance	Character
Hydrogen bonding	$\approx$ 0.05-0.7 eV	$\approx$ 1.5-3.5Å	Selective, directional
Electrostatic ionic	$\approx$ 0.05-2.5 eV	Long range	Nonselective
van der Waals	$\approx$ 0.02-0.1 eV	<1nm	Nonselective
Metal-ligand interactions	$\approx$ 0.5-2 eV	$\approx$ 1.5-2.5Å	Selective, directional

The self-assembly of molecules can be studied using scanning tunneling microscopy in both ultra-high vacuum conditions on metal surfaces as well as at the solid-liquid interface. Below, the basic principles behind molecular self-assembly are summarized, based on the review paper by Kühnle.[36]

In molecular self-assembly the molecules act as building blocks that interact weakly with each other. A relatively weak interaction allows for both the formation and breaking of bonds until an equilibrium state in reached. The formation of molecular structures on surfaces is dependent on the interplay of intermolecular and molecule-substrate interactions. By varying the substrate temperature, the kinetic energy, and therefore the diffusivity, of the molecules is varied. With sufficient kinetic energy E_{kin}, the molecules can overcome the diffusion barrier E_{dif}. Overcoming the diffusion barrier is a prerequisite for the formation of stable structures. Naturally, the kinetic energy should not be greater than the binding energy E_{bin} of the molecules on the surface. A greater kinetic energy leads to desorption of the molecules from the surface. The intermolecular interaction energy E_{inter} contains the information of the molecular building blocks on how to assemble into ordered structures. In the case of a low E_{inter} the molecular building blocks are able to identify the equilibrium state. When this energy is too high the molecules bond irreversibly, preventing the formation of an ordered structure. Thus, the intermolecular interaction energy should be of the order of the kinetic energy. The energy condition for molecular self-assembly on surfaces can be summarized as follows:

$$E_{bin} > E_{inter} \geq E_{kin} > E_{dif} \tag{8}$$

The resulting structure is not only dependent on the interplay of molecule-molecule, molecule-substrate interactions but also, among others, molecular coverage. Below several of these molecule-molecule interactions that need to be considered are described.

2.2.1.1 Intermolecular interactions

An overview of the intermolecular interactions that need to be considered in molecular self-assembly can be found in Table 1.

Hydrogen bonding Hydrogen bonding is defined as an attractive interaction between a hydrogen atom that is covalently bound to a more electronegative group than the hydrogen itself and an atom or group of atoms that is more electronegative, too.[38] The covalently bound group pulls the electron of the hydrogen towards the group, leaving the hydrogen atom positively charged. The positively charged hydrogen atom can then bind with a more electronegative group. From this we can understand that this bonding motif is both selective and directional. The bonding can be both intermolecular and intramolecular. Hydrogen bonding occurs frequently in self-assembly, see for example Refs. [39–43]

Halogen bonding Halogen bonding occurs when a compound R-X, where X is a halogen and R is a covalently bound group to that halogen, has a net attractive interaction between a positively charged region on the halogen and a negatively charged region on another halogen in another or the same group.[44] The positively and negatively charged regions on the halogen are a result of the electrostatic potential.[45, 46] Brinck *et al.* calculated the electrostatic potentials of several different halogen compounds using:

$$V(\mathbf{r}) = \sum_A \frac{Z_A}{|\mathbf{R_A} - \mathbf{r}|} - \int \frac{\rho(\mathbf{r}')dr'}{|\mathbf{r}' - \mathbf{r}|} \tag{9}$$

at position $\mathbf{r}$, where Z_A is the charge on nucleas A, $\mathbf{R}_A$ is the position of nucleus A and $\rho(\mathbf{r})$ is the molecule's electronic density. The first term on the right hand side gives the contribution of the nuclei and the second term gives the contribution of the electrons. A larger nuclei term gives a positive region on the otherwise negatively charged potential surface. See for example the calculated electrostatic potential of 4BrPhM in Figure 7a. The electrostatic potential can also be determined experimentally using diffraction methods.[47] The positively charged region on the molecule is called the σ-hole, and its interaction is highly directional along the extension of the covalent bond.[48] The size of the positive region increases as the atoms become heavier, because the
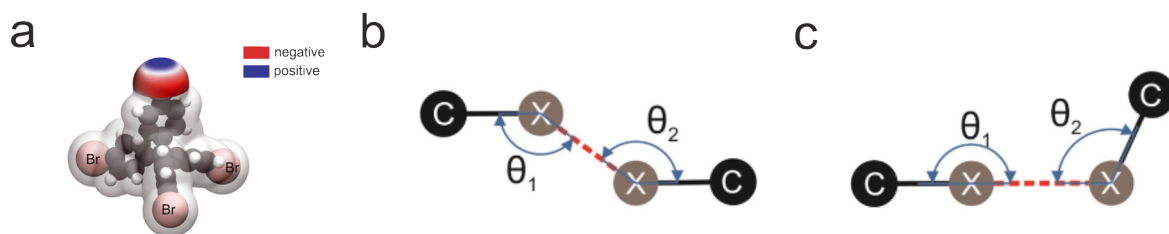
Figure 7: *a) The calculated electrostatic potential of 4BrPhM. The electrostatic potential of the outermost Br atom is shown, which reveals the σ-hole on the Br atom. Adapted from Ref. [49]. b) Two halogenated compounds interacting in a head-on manner, meaning their interaction is repulsive. Adapted from Ref. [50]. c) Two halogenated compounds interacting in a side-on manner, meaning their interaction is attractive. Adapted from Ref. [50].*

Figure 8: *Similarities between a Lewis acid-base reaction (left) and a metal-ligand reaction (right). Adapted from Ref. [66]*

covalently bound group attracts more electrons.[48] Recently, the σ-hole in a halogen compound has been imaged using Kelvin probe force microscopy by Mallada *et al.*[49]

In the case of multiple compounds that contain a halogen, there can be a halogen-halogen interaction, otherwise called halogen bonding or X-bonding. Depending on the angle between the halogens of the different compounds, the interaction can be either repulsive or attractive, see Figures 7b and 7c, respectively. When the similarly charged areas of the halogens point towards each other there is a repulsive interaction. A repulsive interaction occurs when the halogens interact head-on. An attractive interaction occurs when the halogens attract in a side-on manner, so that no similarly charged areas of the halogens point towards each other.[50] Examples of halogen bonding in molecular self-assembly include Refs. [50–53]

Van der Waals interactions Van der Waals interactions describe attractive or repulsive forces between molecular compounds that are not due to bond formation or electrostatic interaction.[54] There are three different kinds of interactions: dipole-dipole, dipole-induced dipole and instantaneous induced dipole-induced dipole (London dispersion force). The dipole-dipole interaction is an intermolecular or intramolecular interaction between compounds that have a permanent electric dipole moment. It can be both attractive and repulsive and depends on the distance and relative orientation of the dipoles. In the second kind of interaction, dipole-induced dipole, a permanent dipole induces a dipole in another compound and with that inducing an attractive interaction. Lastly, the London dispersion force is an attractive force between apolar molecules, due to their instantaneous fluctuating dipole moment. The London dispersion force is proportional to the polarizability of a molecule. Some examples of van der Waals interactions in molecular self-assembly include Refs. [55–60]

Metal-ligand coordination In metal-ligand coordination a metal atom that is supplied or an adatom from the surface reacts with ligands from a molecule, binding the two together. Metal-ligand interactions are similar to Lewis acid-base reactions, see Figure 8. A Lewis acid (base) is a molecular entity that accepts (donates) an electron-pair, making a bond with a Lewis base (acid) through the now shared electron pairs.[54] Metal-ligand coordination is both selective and directional. Furthermore, the bond energies involved help to obtain robust structures.[37] Some examples of metal-ligand coordination in self-assembly are Refs. [1, 61–65].

2.3 On-surface synthesis

2.3.1 Ullmann(-type) coupling

Ullmann coupling was first demonstrated by Fritz Ullmann in 1901 with the synthesis of various biphenyls from aryl halides[3].[67, 68] In this reaction two aryl halides couple to form one biaryl, catalysed by a fine Cu

---

[3]An aryl halide is an aromatic molecule in which one or more of the hydrogen atoms are substituted by a halide.
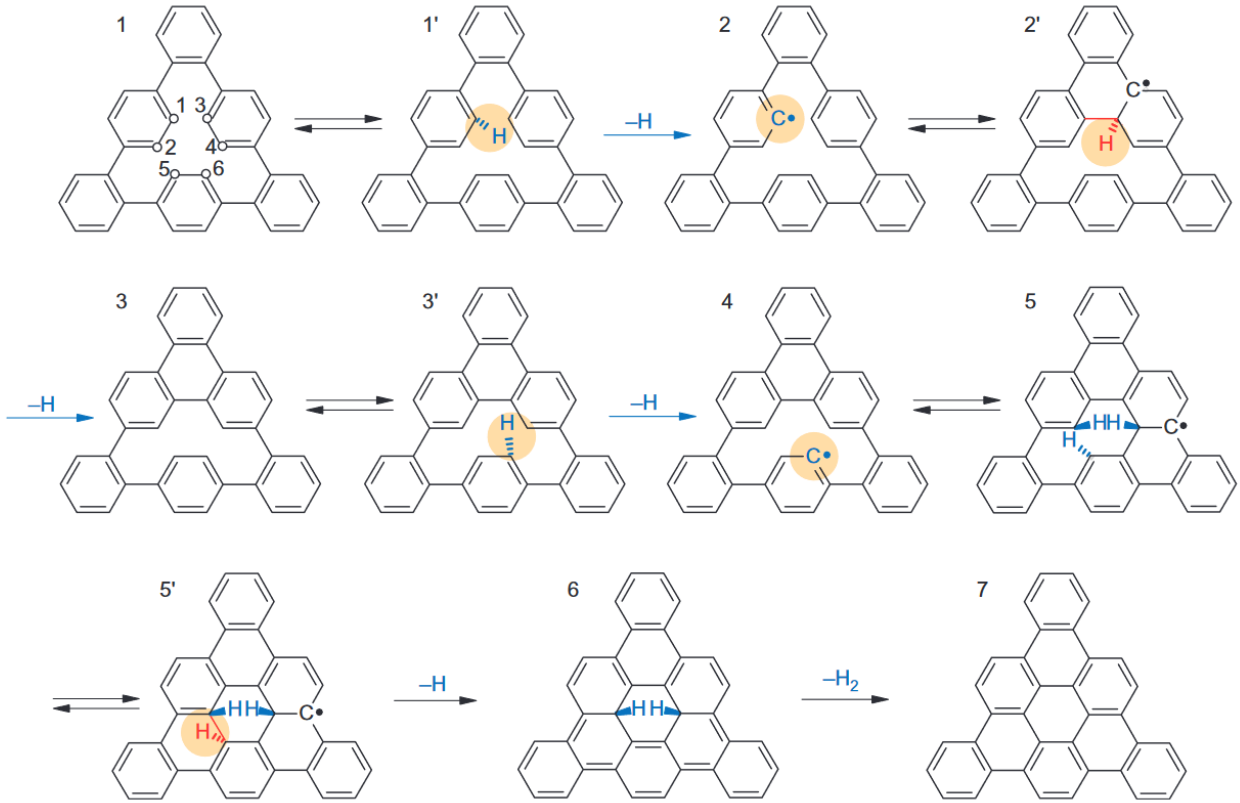
Figure 9: *The reaction path of a polymer intermediate resulting from aryl-aryl coupling reactions on Cu(111) according to DFT simulations by Treier et al.[34] Red indicates the rotation of a dehydrogenated phenylene-ring forming a C-C bond and the subsequent removal of another hydrogen, catalysed by copper. Structures depicted with a primed number are neither stable intermediates nor transition states, and were only found in DFT calculations. The yellow circles indicate catalytic activity from the Cu(111) substrate. Adapted from Ref. [34]*

powder. The pioneering work of Grill *et al.* showed that Ullman-type[4] coupling can be used to form covalently bound nanostructures on surfaces upon annealing.[9] This generally happens in three steps.[69] Firstly, the halogen is separated from the aryl halide, leaving a surface-stabilized radical. Secondly, the surface-stabilized radical diffuses across the surface. Lastly, the radicals combine to form a polymer. Because this coupling scheme generally does not have by-products and the formed polymer has the correct geometry to form GNRs (depending on the chosen precursor molecule) it is very well suitable for the on-surface synthesis of GNRs. The surface acts both as a template and a catalyst by reducing the energy barriers and thus decreasing the dehalogenation temperature, while leaving the surface unaltered. Different surfaces have different reactivities, generally Cu(111) is more reactive than Ag(111), which is again more reactive than Au(111).[70–72]

Several GNRs have already been synthesized on different surfaces through Ullman-type coupling and subsequent cyclodehydrogenation, see for example Refs. [1, 15, 20–25] and recent review papers Refs.[73–75]

2.3.2 Cyclodehydrogenation

The polymer intermediates that are left from Ullman-type coupling of the precursor molecules reach the final GNR configuration via cyclodehydrogenation. Cyclodehydrogenation is an intramolecular reaction that couples the phenyl rings of the intermediates by splitting of H atoms upon annealing. Treier *et al.* investigated the step-by-step process of surface-assisted cyclodehydrogenation of a polyphenylene (CHP) on Cu(111) using DFT calculations and STM.[34] They found five reaction intermediates, which are depicted as 2 to 6 in Figure 9. Reaction intermediates 2, 4 and 5 were found in the DFT calculations, but not in the STM images. The reaction intermediates can be reached via three subsequent mechanisms: (*i*) the removal of a hydrogen which is catalysed by copper, (*ii*) the rotation of the now dehydrogenated phenylene ring towards a neighbouring phenylene ring to form a C-C bond and subsequently the removal of another hydrogen, again catalysed by copper, (*iii*) recombinative H_2 removal. To appreciate the full reaction path in more detail, we refer to the work of Treier *et al.*[34]

---

[4]In this case we call the coupling Ullmann-type, as the coupling is catalysed by surface adatoms instead of a fine Cu powder.

Cyclodehydrogenation is an important step in the fabrication of GNRs, and has therefore been studied specifically for the case of GNRs. Using DFT calculations of 10,10'-dibromo-9,9'-bianthryl (DBBA) on Au(111), Björk *et al.* found that cyclodehydrogenation starts at one end of the ribbon and propagates in a domino-like fashion towards the other end.[70] This is the result of a lower energy barrier for cyclodehydrogenation of a position if the neighbouring positions are already dehydrogenated. That means it is more energetically favourable for a site to cyclodehydrogenate next to a site that is already dehydrogenated. Furthermore, Talirz *et al.* found using STM simulations that the hydrogen that is released during cyclodehydrogenation passivates the carbons at the end of a ribbon.[76] This ends the growth of the ribbons and suggests that the ribbon cannot increase in length after cyclodehydrogenation.

2.4 Precursor molecule 6,12-dibromochrysene

The chosen precursor molecule for this thesis is 6,12-dibromochrysene (DBCh). This molecule is prochiral in the gas and liquid phase, meaning that it can be converted from chiral to achiral in a single step.[1] It can adsorb on a surface face-up or face-down, giving a left- or right-handed enantiomer, both depicted in Figure 6a.

Interestingly, it was shown by Pham *et al.* that the chiral-selectivity of the molecule determines if a cGNR is obtained.[1] On Au(111) the molecule self-assembled into a porous network upon deposition at room temperature (RT). Upon annealing the network at 200°C, a polymer with variable lengths was formed along the herringbone reconstruction of the Au(111) surface. The polymer has a zigzag shape which is due to alternating left- and right-handed DBCh molecules, see Figure 6b. Using DFT calculations, it was confirmed that this coupling scheme is most energetically favourable. Furthermore, the length of the unit cell found using DFT calculations was in good agreement with the experimentally obtained value of 1.4 ± 0.1nm. By annealing the polymers at 350°C GNRs were formed through cyclodehydrogenation, see Figure 6d. To demonstrate the influence of the substrate, Pham *et al.* deposited DBCh on Cu(111), too. The reactivity of Cu surfaces is generally higher than that of Au.[70–72] Now, the molecule formed an 1D polymer. Furthermore, the Cu surface showed vacancies, of which the depth was in agreement with a monoatomic step of the Cu(111) surface. These vacancies indicate the incorporation of Cu adatoms in the polymer. This was confirmed using DFT calculations, as the monomer-to-monomer distance was found to be in good agreement with the measured values of 1.0 ± 0.1nm. Furthermore, DFT calculations showed that chiral Cu-coordinated polymer is the most energetically favourable option. The Cu-coordinated 1D polymer that consists of either left- or right-handed DBCh is depicted in Figure 6c. Upon annealing the Cu-coordinated polymers at 250°C, no GNRs were obtained. It is concluded that the difference in bond formation (covalent versus metal-organic) is the main reason for the chiral selectivity. This chiral selectivity is in turn the reason that GNRs were formed on Au(111) but not on Cu(111).

The GNRs formed on Au(111) were studied in more detail by Houtsma *et al.* using STM and STS.[69] These techniques will be explained in more detail in Chapter 3. Similarly to Pham *et al.* not only straight GNRs were observed, but also cross-linked ribbons. A higher amount of cross-linked ribbons was found for higher annealing temperatures and longer annealing times. Another defect was observed, where instead of the coupling scheme described above (alternating left- and right-handed enantiomers), two enantiomers of the same chirality coupled. This was seen in the STM images as two bright protrusions, which are likely due to steric repulsion. At higher annealing temperatures, these groups lie in the same plane as the GNR. This is likely accommodated by further dehydrogenation, which forms two five-membered carbon rings. In addition, the electronic properties of the GNRs were studied with the use of STS. The difference between the highest occupied molecular orbit (HOMO) and lowest occupied molecular orbit (LUMO) was found to be 1.3 ± 0.1eV. The measured bandgap was in reasonable agreement with DFT calculations. Furthermore, using differential conductance mapping, it was shown that the states of the GNR appear mostly around the edges.

3 Experimental methods

3.1 Scanning tunneling microscopy

In 1981 Binnig and Rohrer invented the scanning tunneling microscope [77], an instrument that probes the surface topology[5] and electronic properties of a conducting sample using an atomically sharp tip. The tip, usually made of Pt/Ir or W, is brought within a few Ångströms of the sample surface and is scanned parallel to the surface with the use of piezoelectric elements. A bias voltage is applied between the tip and sample, causing a directed tunneling current to flow. This tunneling current depends on the applied voltage and the overlap of the local density of states (LDOS) of both the tip and sample, as well as exponentially on the distance between tip and sample. In the following sections, the theoretical understandings behind tunneling and the STM are discussed in more detail.

3.1.1 Quantum tunneling

As described above, when a bias voltage is applied between tip and sample, a directed tunneling current will flow. Thus, to understand the theoretical workings of the microscope, we need to understand quantum tunneling. Quantum tunneling describes the phenomenon in which particles are able to pass through a classically forbidden region.[78] To describe this phenomenon, we consider three regions as depicted in Figure 10. Regions **a** and **c** are classically allowed regions separated by a classically forbidden region **b** of width L. Regions **a** and **c** describe the tip and sample, whereas region **b** describes the vacuum gap between tip and sample.

Consider an electron with energy E incident on the potential barrier with potential V_0 in region **b**. The electron is described by the time-independent Schrödinger equation,

$$-\frac{\hbar^2}{2m}\frac{\partial^2\psi(x)}{\partial x^2} + U(x)\psi(x) = E\psi(x), \tag{10}$$

where $\hbar$ is the reduced Planck's constant, m is the electron mass, $U(x)$ is the potential, $\psi(x)$ is the wavefunction of the electron and E is the energy of the electron. From Schrödinger's equation it can be seen that the solution for the wavefunction has to be twice differentiable, meaning it and its derivative have to be continuous. Solutions to the Schrödinger equation can be written as $\psi = const. \exp(\pm ikx)$, where forward travelling waves are described with a positive sign and backward (reflected) waves with a negative sign. The wavefunctions in the allowed regions are:

$$\psi_{\mathbf{a}}(x) = A\exp(ikx) + B\exp(-ikx) \tag{11}$$

and

$$\psi_{\mathbf{c}}(x) = F\exp(ikx), \tag{12}$$

where A, B and F are constants which can be found using the appropiate boundary conditions and $k = \sqrt{2mE/\hbar^2}$. The wavefunction in region **b**, the classically forbidden region, is given by:

$$\psi_{\mathbf{b}}(x) = C\exp(\kappa x) + D\exp(-\kappa x), \tag{13}$$

where C and D are constants and $\kappa = \sqrt{2m(V_0 - E)/\hbar^2}$. When solving the Schrödinger equation for $V_0 > E$, we have $ik = \sqrt{2m(E - V_0)/\hbar^2}$. Naturally, the growing solution is not allowed in the forbidden region, as the amplitude cannot grow in the forbidden region. This means the electron tunnels through the potential barrier with an exponentially decaying wavefunction. When the barrier is narrow (small L), the probability of finding the electron in region **c** is reasonable.

By observing that the wavefunction and its derivative have to be continuous at the boundaries of each zone the constants A, B, C, D and F can be found. Furthermore, the probability T for a tunneling event to happen can be calculated from the square of the amplitude transmission coefficient F [78]:

$$T = \frac{1}{1 + (V_0^2/4E(V_0 - E))\sinh^2(\kappa L)}, \tag{14}$$

where L is the thickness of the barrier. For small tunneling rates, we have $2\kappa L \gg 1$, meaning the sinh function can be approximated by an exponential function. This gives a simpler expression of the transmission coefficient T:

$$T \approx \frac{16(V_0 - E)}{V_0^2}\exp(-2\kappa L), \tag{15}$$

from which it can be seen that the transmission probability is a function of the barrier width L. Because region **b** describes the vacuum, the barrier width describes the tip-sample distance. Thus, the transmission probability

---

[5]The surface topology itself is not probed, rather a map of constant local density of states is measured. This will be explained in more detail in the sections below.
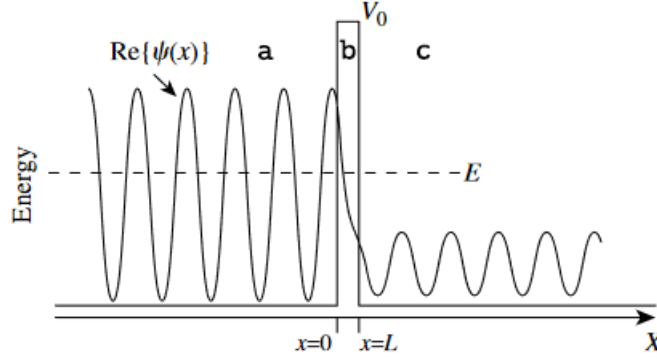
Figure 10: *Schematic depicting the model for quantum tunneling through a classically forbidden region. Region **a** and **c** are classically allowed regions. Region **b** is the classically forbidden region of width L, because the potential V_0 is greater than the energy of the electron E. The real part of the wavefunction is shown, from which it can be seen that the probability of finding the electron exponentially decays in region **b** and is nonzero in region **c**. Adapted from Ref. [78]*

depends exponentially on the tip-sample distance. To show how sensitive the transmission probability is to changes of the tip-sample distance, consider the workfunction[6] of a single crystal of Ag(111) $\phi = V_0 - E = 4.74\text{eV}$.[78, 80] This gives $\kappa = 1$ Å^{-1}, meaning the transmission coefficient has a decay constant of 2Å^{-1}. Evidently, the transmission probability, and therefore the tunneling current, is sensitive to changes in the tip-sample distance.

3.1.1.1 Tunneling in STM

Now, that the tunneling principle is understood, we can apply it to the case of the STM. There is only a net tunneling current when a bias voltage is applied between the tip and sample. The electron can tunnel from the tip to the sample and *vice versa*. When the tip is grounded and the bias voltage is applied to the sample, we speak of a sample voltage. For a positive bias voltage, the electrons will tunnel from the occupied states of the tip to the empty states of the sample. Whereas, for a negative bias voltage, the electrons tunnel from occupied states in the sample to empty states in the tip, see Figure 11a. Assume an electron with an energy of ε and an applied bias voltage $-V$, where $E_F - eV < \varepsilon < E_F$. The electrons of the states between $E_F - eV$ and E_F have a chance to tunnel to the tip, as can be seen in Figure 11a. The probability of the electron to be found at the tip is:

$$P \propto |\Psi(0)|^2 \exp(-2\kappa L), \tag{16}$$

where 0 is the position of the sample surface and L is the tip-sample distance. By summing over all the states with energy $E_F - eV < \varepsilon < E_F$, the tunneling current is found to be [79]:

$$I \propto \sum_{\varepsilon = E_F - eV}^{E_F} |\Psi(0)|^2 \exp(-2\kappa L) \tag{17}$$

If the applied bias voltage V is small enough, the density of electronic states does not vary significantly, meaning we can write the tunneling current as a function of the LDOS[7]. At tip location z and energy E, the LDOS of the sample is given by:

$$\rho_s(z, E) \equiv \frac{1}{eV} \sum_{E = E - eV}^{E} |\psi_n(z)|^2 \tag{18}$$

Therefore, the tunneling current of the STM can be written as:

$$I \propto V \rho_s(0, E_F) \exp(-2\kappa L) \tag{19}$$

From Equation 19 it is evident that the tunneling current is sensitive to the tip-sample distance. Furthermore, the tunneling current scales with both the bias voltage and the density of states. This means that when keeping the bias voltage constant, the STM can image the LDOS of the sample, which can be interpreted as a topology map of the sample.

---

[6]The workfunction of the surface of a metal is as defined the minimum energy required to remove an electron from the bulk to the vacuum level.[28, 79]

[7]The LDOS is the number of electrons per unit volume per unit energy, at a given point in space and at a given energy.[79]
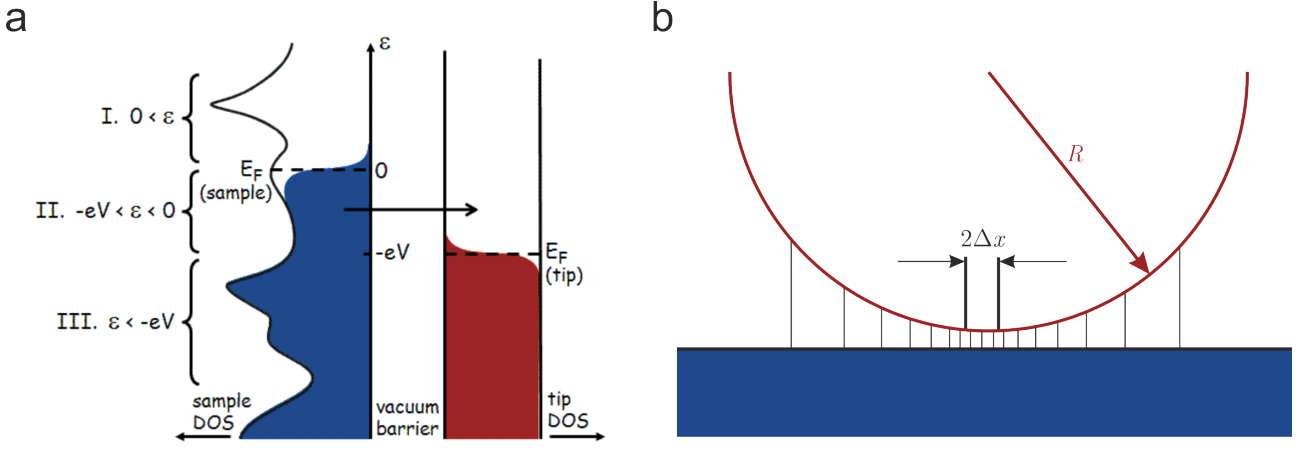
Figure 11: *a) The density of states of the sample (left) and the tip (right) seperated by a vacuum. A negative bias voltage is applied between the tip and sample. In region I no tunneling occurs because there are no filled states in the sample. In region II, tunneling occurs because there are filled states in the sample which can tunnel to the unfilled states in the tip. In region III, no tunneling occurs because there are no available states in the tip. Adapted from Ref. [81]. b) Schematic representation of the tip (red) and sample surface (blue) depicting the tunnel current lines. The tunnel current lines are concentrated in a small region around the apex of the tip and are approximately perpendicular to the sample surface. Based on Ref. [79]*

3.1.2 Lateral resolution in STM

Binnig and Rohrer initially predicted that the lateral resolution would be much smaller than the radius of the tip. They assumed that when the tip-sample distance is small enough, the tunnel current lines are approximately perpendicular to the sample surface at the apex of the tip, see Figure 11b. At a point Δx on the tip, the distance to the sample surface Δz is increased by:

$$\Delta z \approx \frac{\Delta x^2}{2R} \tag{20}$$

By assuming that at each point the tunneling current follows Equation 15, we find the following lateral current distribution[79]:

$$I(\Delta x) = I_0 \exp\left(-2\kappa \frac{\Delta x^2}{2R}\right), \tag{21}$$

where κ is the decay constant, Δx is the distance between lateral current lines and R is the tip radius. Using typical numbers $\kappa \approx 1$ Å^{-1}, $R \approx 1000$Å and $\Delta x \approx 45$Å, the lateral current distribution drops by approximately one order of magnitude in comparison with the tip radius. For a tip radius of $R \approx 100$Å, the current concentrates in a circle of approximately 14Å, thus underestimating the actual resolution of an STM.

3.1.3 Bardeen's formalism

Bardeen formulated a more sophisticated solution to the tunneling current. In his approach he did not solve the Schrödinger equation of the complete system but instead considered two separate systems using time-dependent perturbation theory.[79, 82] The two systems (electrodes) are separated by an insulating barrier. He showed that the amplitude of the electron transfer is determined from the overlap between wavefunctions of the two electrodes. If the temperature is low enough ($k_B T$ smaller than the energy resolution required by the experiment), the tunneling current is given by:

$$I = \frac{4\pi e}{\hbar} \int_0^{eV} \rho_S(E_F - eV + \epsilon)\rho_T(E_F + \epsilon)|M|^2 d\epsilon, \tag{22}$$

where V is the applied bias voltage between the electrodes, M is the tunneling matrix element[8], ρ_S the DOS of the first electrode (sample) and ρ_T the DOS of the second electrode (tip).

3.1.4 The spherical-wave-tip model

The nearly atomic resolution of the STM prompted researchers to understand the imaging mechanism and the resolution in more detail. A widely used model for understanding the resolution of the STM is that of Tersoff and Hamann.[83] The apex of the STM tip is modelled as a sphere with a radius of curvature $\mathbf{r}_0$. By solving

---

[8]The tunneling matrix element describes the amplitude of the electron transfer.
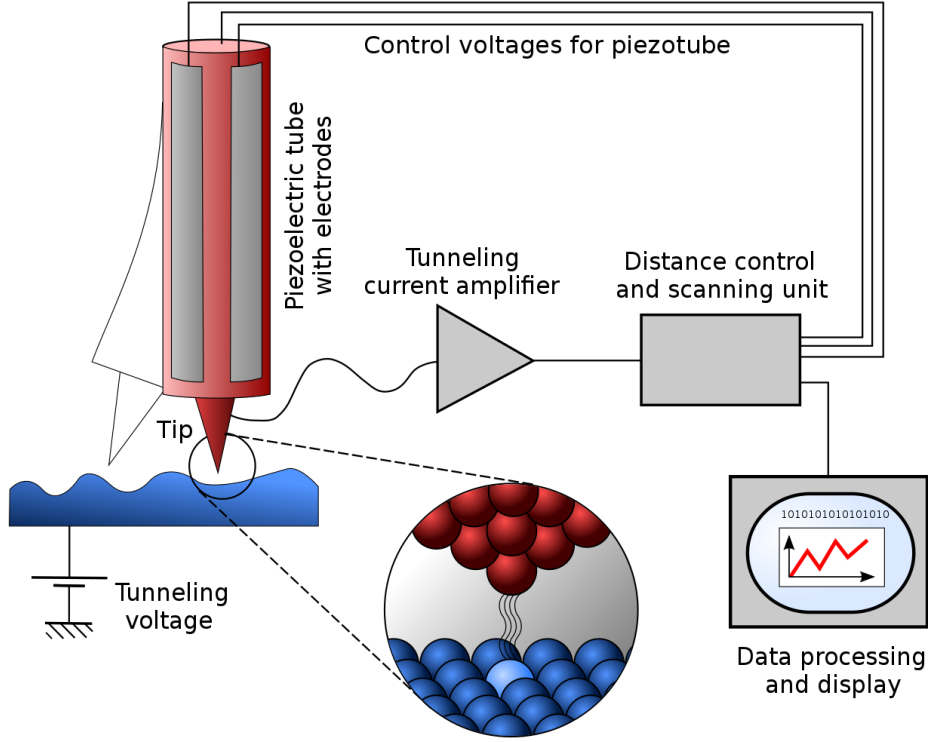
Figure 12: *A schematic representation of the STM. Adapted from Ref. [78]*

Schrödinger's equation for a spherical potential well of radius R the wavefunctions of the tip are found. Tersoff and Hamann assumed that only the spherical-wave solution was of importance. This is why it is called the s-wave tip model. This means that the properties of the tip can be taken out of the problem and only the properties of the surface matter. At a low bias voltage, the tunneling current is found to be proportional to the LDOS ρ_v directly beneath the centre of the tip:

$$I \propto \sum_{E=E_F-eV}^{E_F} |\Psi(\mathbf{r}_0)|^2 = eV\rho_S(\mathbf{r}_0, E_F) \tag{23}$$

This means that a constant-current measurement (see Section 3.1.5 for more detail on this) is a contour of the LDOS of the surface of the sample. In the case of free-electron metals, the images are the surface charge-density contours. The spherical-wave-tip model is not able to explain the atomic resolution of an STM. It was later found by Tersoff and Lang that the tip electronic states have large effects on STM images of atomic-size features, in particular on graphite.[84] Chen *et al.* were able to explain the observed atomic resolution of the STM by extending the s-wave-tip model by considering the p- and d-wave solutions of the Schrödinger's equation, which were omitted by Tersoff and Hamann.[85]

3.1.5 Operating modes

In the previous sections it is shown that the tunneling current between tip and sample is proportional to the applied bias voltage, the LDOS and the tip-sample distance. Now, the operation principle of the STM can be discussed. The atomically sharp tip can be scanned along the surface in the x-, y- and z-directions with the use of piezoelectric elements, see Figure 12.

The STM can be operated in two different modes, constant current mode and constant height mode. By operating the STM in constant current mode the current is kept constant with the use of a feedback loop that regulates the tip-sample distance. When operating the STM in constant height mode the tip is kept at a constant distance from the sample by keeping the voltage at the z-piezoelement constant and the current is recorded at every position. Now, from Equation 23 it is understood that a height profile can be found from the current profile recorded. The advantage of constant height mode is that no feedback loop is required, making measurements quicker. However, this does come at the risk of crashing into the sample and possibly damaging it.
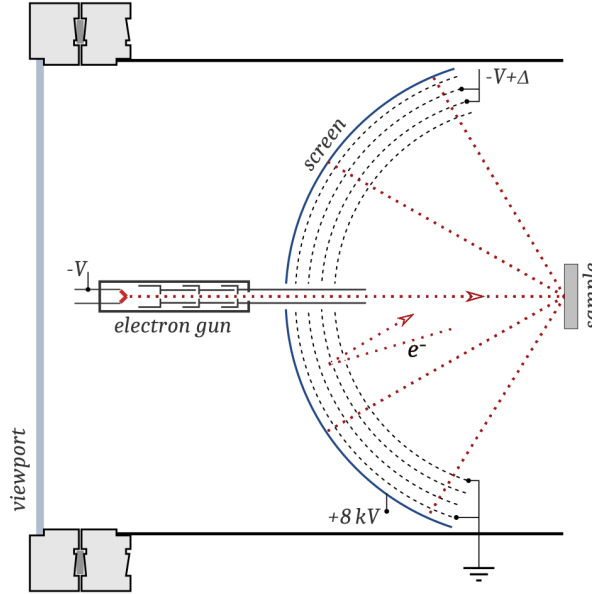
Figure 13: *A schematic representation of a LEED-setup. Based on Ref. [90]*

3.2 Scanning tunneling spectroscopy

A technique related to STM is scanning tunneling spectroscopy. In scanning tunneling spectroscopy (STS) the electronic properties (e.g. the bandgap) of a sample can be probed by keeping the tip at a fixed position and recording the tunneling current as a function of the bias voltage, giving the I-V curve of the chosen location. Equation 19 shows that the tunneling current is dependent of both the DOS of the sample and the DOS of the tip. By assuming that the tunneling matrix element M does not change significantly on the energy interval of interest, the tunneling current can be expressed as:

$$I \propto \int_0^{eV} \rho_S(E_F - eV + \epsilon)\rho_T(E_F + \epsilon)d\epsilon \tag{24}$$

Which shows that in this case the DOS of the sample and the DOS of the tip contribute equally to the tunneling current, which was experimentally verified using a different arrangement of the electrodes by Giaever *et al.* in 1961.[86] Thus, in order to probe the DOS of the sample, the DOS of the tip must be constant. This is achieved by using a metallic tip, so Equation 24 implies that:

$$\frac{dI}{dV} \propto \rho_S(E_F - eV) \tag{25}$$

Which shows that the differential conductivity is proportional to the DOS of the sample. The metallic tip used in STM needs to be treated to be able to take STS spectra.[87, 88]

Because the tunneling current depends on both the applied bias voltage and the tip-sample distance, it will vary with approximately one order of magnitude per Ångström. Because the variation of the tunneling current is of more interest than the absolute value, normalization is a simple solution to this problem. Feenstra *et al.* proposed a normalization of the differential conductivity by dividing the differential conductivity by I/V.[87, 88]

3.3 Low-energy electron diffraction

Another way of studying the structure of a surface is low-energy electron diffraction (LEED), in which the surface is bombarded with a collimated beam of low-energy electrons (30eV to 200eV). The electrons scatter elastically on the surface and are redirected to a fluorescent screen, showing the diffraction pattern (LEED-pattern) of the structuret. A schematic of the setup is depicted in Figure 13. The LEED-pattern seen on the fluorescent screen contains information -among others- on periodic molecular structures and the crystal lattice.[89]

The low-energy electrons used in LEED typically have an energy that ranges from 30eV to 200eV, which is chosen for two reasons. Firstly, it means that their *de Broglie* wavelength,

$$\lambda = \frac{h}{\sqrt{2mE}}, \lambda[\mathring{A}] = \sqrt{\frac{150}{E(eV)}} \tag{26}$$
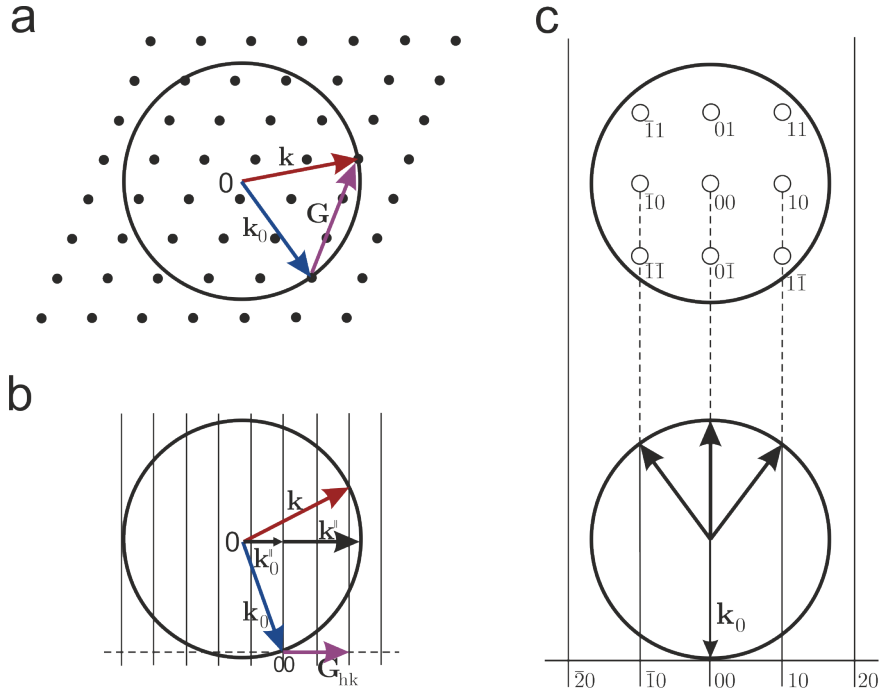
Figure 14: *a) Construction of the Ewald's sphere using a reciprocal lattice. b) Construction of the Ewald's sphere for diffraction on a 2D surface. c) Labelling of the LEED-pattern at normal incidence. The spots are labelled using the same indexing as that of a reciprocal lattice. Based on Ref. [89]*

lies in the range of $1 - 2$Å. Because the *de Broglie* wavelength is of the order of the interatomic distances studied, it satisfies the diffraction condition[9]. Secondly, the mean free path of electrons is short. This means that electrons are more likely to lose energy due to the scattering events with deeper lying layers and thus, are not relevant for the diffraction pattern. Therefore, LEED is well suited for studying the 2D atomic structure of a sample surface.

The diffraction pattern of the electrons is directly related to the reciprocal lattice of the crystal by the following condition:

$$\mathbf{k} - \mathbf{k}_0 = \mathbf{G}_{hkl} \tag{27}$$

where $\mathbf{k}_0$ is the incident wave vector, $\mathbf{k}$ is the scattered wave vector and $\mathbf{G}_{hkl}$ is the reciprocal lattice vector. In the case of elastic scattering:

$$|\mathbf{k}| = |\mathbf{k}_0| \tag{28}$$

Thus we have conservation of momentum (Equation 27) and conservation of energy (Equation 28).

Using the Ewald's sphere construction, the diffraction pattern can be represented graphically, see Figure 14a. The sphere is constructed on the reciprocal lattice of the crystal. In the lattice the incident wave vector $\mathbf{k}_0$ is drawn in such a way that its end lays on a reciprocal lattice point, see Figure 14a. Then a sphere of radius $k = 2\pi/\lambda$ is centered at the origin of the incident wave vector. The reciprocal lattice points that lie on the surface of the sphere are the scattered wave vectors $\mathbf{k}$. In the case of diffraction on a surface, Equation 27 becomes:

$$\mathbf{k}^{||} - \mathbf{k}_0^{||} = \mathbf{G}_{hk} \tag{29}$$

meaning that now only the wave vector components parallel to the surface need to be equal to the reciprocal wave vector $\mathbf{G}_{hk}$. The wave vector components perpendicular to the surface do not need to be conserved. The 2D lattice can be found from the 3D lattice with infinite periodicity in the normal direction, meaning the lattice vector goes to infinity. As the lattice vector goes to infinity, the wave vector goes to zero, meaning the reciprocal lattice points along the normal direction are infinitely dense. This means that the construction of the Ewald's sphere is now easier, as now we have reciprocal lattice rods instead of points, see Figure 14b. The incident wave vector $\mathbf{k}_0$ now terminates at a lattice rod instead of point. The scattered wave vectors are now the intercepts of the Ewald's sphere with the rods.

The diffraction pattern seen at the viewport (behind the fluorescent screen) is a measure of the surface reciprocal lattice. The fluorescent screen can be seen as the surface of the Ewald's sphere and the diffracted electrons produce spots where the reciprocal lattice rods intersect the Ewald's sphere. The number of spots in the LEED-pattern depends on the size of the Ewald's sphere. By increasing the energy of the electrons, their

---

[9]The diffraction condition is $n\lambda = 2d\sin\theta$, which is called Bragg's law.[28]
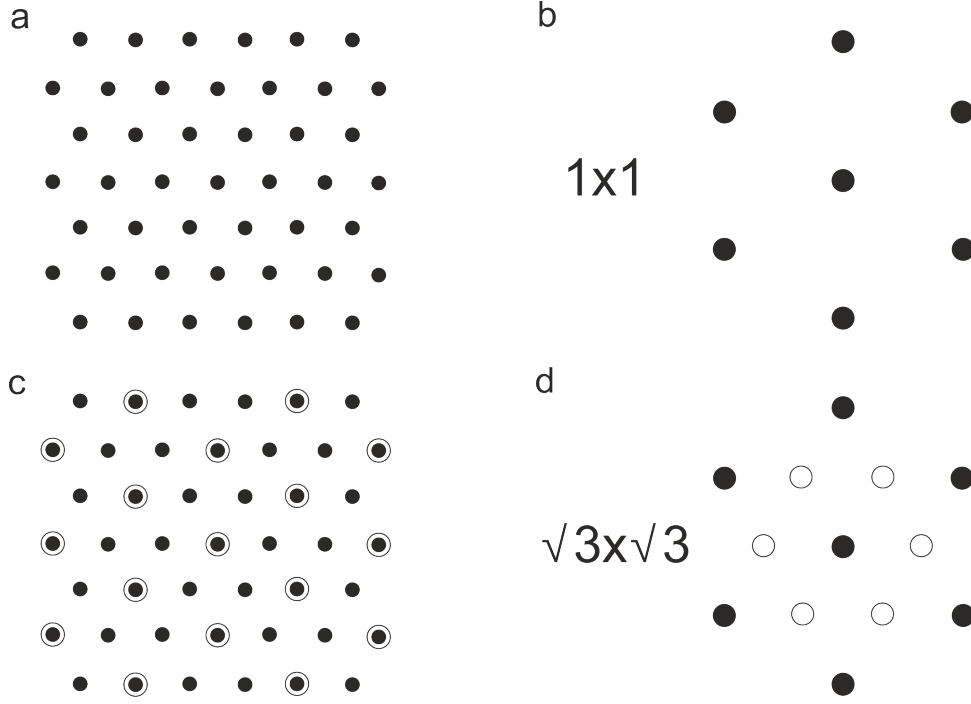
Figure 15: *a) The real space lattice of a substrate with a hexagonal lattice, like Ag(111). b) The corresponding 1x1 LEED-pattern. c) The real-space lattice of a subtrate with a hexagonal lattice plus a superstructure. d) The corresponding $\sqrt{3} \times \sqrt{3}$ LEED-pattern. Main spots are depicted using solid-circles whereas superspots are depicted using circles. Based on Ref. [89]*

wavelength is reduced and consequently the radius of the Ewald's sphere is increased. The diffraction spots now lie closer to the $(0,0)$-spot and more spots are seen on the fluorescent screen. The spots are indexed in the same way as the indexing of a reciprocal lattice. The spot located at the center of the LEED pattern is the $(0,0)$-spot, see Figure 14c.

From the LEED-pattern information on the presence of defects and imperfections of the crystal structure can be deducted by inspection of the sharpness of the spots. A structure with little defects has bright and sharp spots with little background intensity. The spots are broadened and weakened if defects are present in the structure. If no spots are present at all the structure is likely disordered or polycrystalline.

More importantly, the surface 2D lattice can be deducted from the LEED-pattern. We know that Ag has a face-centered cubic crystal structure, meaning its (111)-plane has the real-space lattice given in Figure 15a. By simply finding the reciprocal lattice using Equation 30, we find the LEED-pattern depicted in Figure 15b. The spots that result from the surface are called the main-spots.

$$
\begin{aligned}
\mathbf{a}_s^* &= G_{11}^*\mathbf{a}^* + G_{12}^*\mathbf{b}^* \\
\mathbf{b}_s^* &= G_{21}^*\mathbf{a}^* + G_{22}^*\mathbf{b}^* \\
G^* &= (G^{-1})^T
\end{aligned}
\tag{30}
$$

When a superstructure forms on a surface (e.g. self-assembly of DBCh molecules), new spots, called superspots, are seen in the LEED-pattern. An example of such a superstructure and its LEED-pattern is given in Figures 15c and 15d, respectively.

3.4 Experimental setup

The experiments in this thesis were carried out using a commercially available low temperature STM (Scienta Omicron), which can be seen in Figure 16. The setup consists of two chambers, the STM chamber and the preparation chamber, which are mounted on a table with active damping. The STM chamber hosts the STM and a carousel in which samples can be stored. The chamber is kept at a base pressure of 10^{-11}mbar. The STM itself is suspended in springs and equipped with Eddy current damping[10] to reduce noise. It can be cooled by filling the cryostat on top of the STM with LN$_2$ (77K) or LHe (4.2K). The preparation chamber is equipped with an Ar$^+$ sputter gun, an evaporator for molecules, an evaporator for metals, a LEED chamber and a quartz microbalance (QMB). The preparation chamber has a base pressure of 10^{-10}mbar. The manipulator is used to

---

[10]When a conductor moves in a magnetic field, damping forces are generated by Eddy currents induced in the conductor.[79] This can be used as an active damping system to reduce noise.
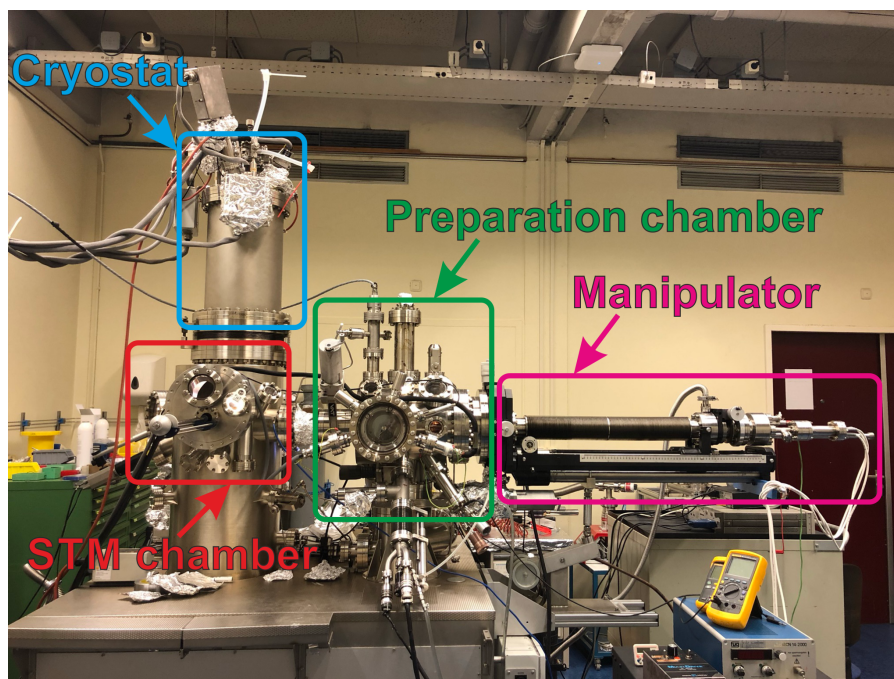
Figure 16: *The low temperature UHV-STM setup used for the experiments in this thesis.*

move samples within the chambers and to transfer between chambers. It is equipped with a filament for resistive heating, which is used to anneal the samples in this thesis. The temperature of the sample on the manipulator is read using a thermocouple. The actual temperature of the sample is roughly double that temperature. The images taken using this setup are analyzed using WSxM. [91]

3.5   Sample preparation

3.5.1   Cleaning the Ag(111) crystal

The Ag(111) single crystal is cleaned with repeated sputtering-annealing cycles. A sputtering-annealing cycle consists of two steps. First, the sample is sputtered with Ar^+ ions in two different angles. The sputtering time per angle is 15 minutes. The Ar^+ ions are directed towards the surface, where they collide with the atoms of the solid surface. As a result, the kinetic energy of the ion is transferred to an atom in the solid. If the kinetic energy transferred to the atom in the solid is higher than the surface binding energy of that atom a recoil atom is produced. This recoil atom will collide with more solid atoms, resulting in a cascade of collisions.[92] The topmost layers of the surface are removed, leaving a rough surface. Following a sputtering cycle, the sample is annealed to smooth the surface. This is done for 45 to 60 minutes using the resistive heating filament on the manipulator. This is repeated twice, but more cycles can be done if the crystal is exceptionally dirty.

3.5.2   Deposition of DBCh molecules

The precursor molecule DBCh is deposited on the clean single crystal using a molecule evaporator. Inside the water-cooled evaporator are crucibles that hold the molecules. By heating the crucible that contains DBCh the molecules evaporate. DBCh starts evaporating around 155°C. The QMB inside the preparation chamber is used to measure the incident flux of material onto the sample, from which the rate (Å/min) can be determined. As the name suggests, the QMB consists of a quartz crystal that is oscillated at resonance frequency. As material is deposited onto the QMB, its resonance frequency shifts, from which the influx of material can be determined.[78]

When the desired rate is reached the QMB is moved out of the way so that the clean single crystal can be brought close to the evaporator, with the surface facing away. Deposition is done by turning the surface of the clean crystal towards the evaporator for the time to reach the desired thickness. When the desired thickness is reached, the crystal is moved out of the way so that the QMB can be brought in the chamber again to measure the deposition rate. By taking the average of the deposition rate before and after the crystal was in place and the deposition time, the thickness can be estimated.

4 Results

In the following sections, the results of this work are presented and discussed. This is done per deposition or post-deposition annealing temperature in Section 4.1. Furthermore, the influence of the deposition rate is discussed in Section 4.1.2.2. An overview of all samples of this work can be found in Table 2 in Appendix A. The samples were made by depositing DBCh on a Ag(111) substrate kept at room temperature or by depositing on a warm sample. The sample is kept at a certain temperature using the resistive heating on the manipulator head. Post-deposition the samples could be annealed using this resistive heating.

4.1 Temperature dependence

4.1.1 Deposition at room temperature

An overview STM image of DBCh on Ag(111) deposited at room temperature is shown in Figure 17. From the image it is clear that there are three distinct self-assemblies, which will be called self-assemblies i, ii and iii. Self-assembly i occurs in fairly small domains and resembles a porous network when imaged using a positve bias voltage. The second self-assembly (ii) appears in large domains as dashes that align parallel to each other in rows. This self-assembly resembles long chains that align parallel to each other when imaged using a negative bias voltage. The last self-assembly found at room temperature, self-assembly iii, resembles dashes that show no order.

Interestingly, it was observed that a small difference in temperature changes the (sizes of) self-assemblies drastically. Deposition at 25°C led to the formation of self-assemblies i, ii and iii. Whereas, deposition at slightly elevated temperatures (31 or 33°C) formed only self-assemblies i and iii. Moreover, the patches of self-assembly i were smaller at these slightly higher temperatures.

4.1.1.1 Self-assembly i

A high-resolution STM image of self-assembly i can be seen in Figure 18a. The image taken with a negative bias shows dashes that form a chevron-like pattern by changing direction every three units and both brighter and dimmer dots. The red box in Figure 18a shows such a unit of three dashes. The dashes do not align parallel to each other, rather there is an angle of approximately 16° between the middle and outer ones. The length of such a unit is approximately 2.5nm, meaning it would fit three DBCh molecules. Therefore, the dashes are attributed to the carbon backbone of a DBCh molecule. Dots can be seen in between the middle and outer ones, as well at the sides of the outer ones. There is only one bright dot in between the middle and outer dashes, indicating that one or both of the DBCh molecules were debrominated. Because there is no attractive interaction between a debrominated DBCh molecule and an intact DBCh molecule, both molecules must be (partially) debrominated. As a result, the bright dot connecting the middle and outer dashes is attributed to a silver adatom that has diffused from the surface. The silver adatom coordinates at the debrominated site of the DBCh molecules. The van der Waals radius of a silver atom is 172pm[93], giving a diameter of 344pm. This is in agreement with the images. Furthermore, assigning the bright protrusions to silver adatoms is consistent with for example the work of Píš *et al.* in which 5,11-dibromotetracene was deposited on Ag(110), which resulted in the formation of organometallic structures which coordinated with silver adatoms and split-off halogens.[94]

The next unit of three can be found almost perpendicular to one of the outer dashes. It can be seen that the end of the carbon backbone of the outer molecule coordinates with a bright dot of the unit in the red box, see the green circles in Figure 18a. Furthermore, with close inspection, a difference in contrast with the outer dashes of a unit can be seen when comparing the bright dots at the outer sides and the inner sides of the dash. Because the carbon backbone can only coordinate with a silver adatom at the debrominated sites of the molecule it can be inferred that the outer molecules of a unit of three are only partially debrominated. This also explains the difference in contrast between bright dots at the inner and outer sides of the outer dashes within a unit of three. The slightly dimmer dots are attributed to silver adatoms for the reasons stated above, whereas the brighter dots are now attributed to Br atoms that are still attached to DBCh molecules.

In short, dashes are attributed to the carbon backbone of a DBCh molecule, the brightest dots to the Br atoms of partially debrominated DBCh molecules and the slightly dimmer dots to silver adatoms that coordinate with debrominated sites. In the image in Figure 18a one can also see dim dots occurring anywhere in the network. These are attributed to Br atoms that were split-off the DBCh molecules in the network. Other examples of split-off halogens that coordinate with the H atoms of their dehalogenated precursor include Refs. [95–97] In the work of Píš *et al.*, the desorption of the split-off Br atoms was investigated. Using XPS at different temperatures it was concluded that the split-off Br atoms do not desorb from the surface until a temperature of 573K is reached. Furthermore, it was discussed that the presence of the split-off Br atoms plays a role in lowering the energy of the formed structures.
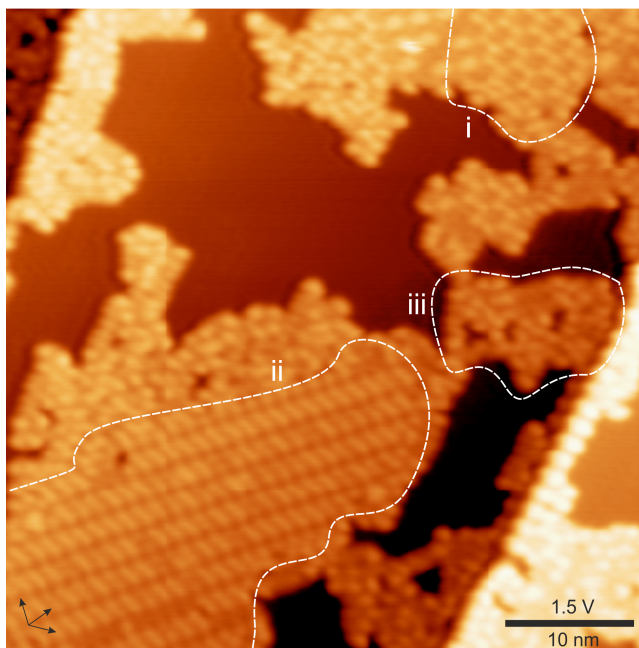
Figure 17: *An overview STM image of deposition of DBCh on Ag(111) at room temperature. The image shows three distinct self-assemblies.* $I = 20pA$, $V = 1.5V$.

With this information, we can construct the unit cell of the network which is given in an overlay in Figure 18a and Figure 18b. The unit cell has parameters $a = 4.36 \pm 0.09$nm, $b = 1.58 \pm 0.07$nm and $\theta = 91.99 \pm 2.18$. Both chiralities of the DBCh molecule are found in the unit cell. Because of the chevron-like pattern formed by the units of three, this self-assembly will be called the chevron-network.

Using the overlay of the unit cell, the carbon-silver-adatom-carbon (C-Ag-C) distance is determined as 0.47 ± 0.04nm. The center-Ag-center distance of one dash to the other is determined as 0.92 ± 0.02nm. Park *et al.* reported on the deposition of 9,10-dibromoanthracene (DBA) on Ag(111) at room temperature.[63] The DBA molecules debrominated upon deposition and formed 2D networks of 1D metal-coordinated chains. The Ag-DBA-Ag distance was 0.73nm, meaning the C-Ag-C distance was 0.45nm. Interestingly, the Br atoms that split-off the DBA molecules filled the empty spaces in between the chains, similar to what is observed in the chevron network. Another example of silver adatom coordination was reported by Fan *et al.*, who deposited 4,4"-dibromo-*m*-terphenyl (DMTP) on Ag(111).[98] Upon annealing to 333K, the DMTP molecules coordinated with a silver adatom. The corner-to-corner distance of a staple-shifted unit (explanation follows) was determined to be 1.6nm (1.59 according to DFT-calculations), meaning a C-Ag-C distance of 0.50nm. Thus, the C-Ag-C distance of the chevron-network is in agreement with the two examples of metal-coordination given above.

Using the overlay of the unit cell, the Br$\cdots$H distance can also be determined. The distance between the Br atom of a partially debrominated DBCh molecule and the closest hydrogen is 0.22 ± 0.04nm. The Br$\cdots$H distance in the chains formed of DBA on Ag(111) in the work of Park *et al.* is 0.28nm or 0.30nm, depending on the apparent height of the DBA molecule. According to DFT calculations this distance should be slighty shorter, 0.27nm and 0.29nm, respectively. Both values are close to the distances measured in the chevron network. Moreover, these are typical lengths for hydrogen bonds, see Table 1.

An example of partial debromination on Ag(111) was found by Fan *et al.* in 2018. In this work, DMTP was deposited on Ag(111) and subsequently annealed to 333K.[98] This resulted in the so-called *staple shift pattern* where partially debrominated DMTP molecules coordinated with a silver adatom on the dehalogonated site. The partial debromination of the DMTP molecules was confirmed by XPS measurements. Because the surface is similar and the temperature is reasonably close to the temperature of the sample above, it is possible that the chevron network also shows partially debrominated molecules. Furthermore, full debromination of a molecule is known to occur at room temperature on Ag(111) in similar molecules, e.g. DBA, DMTP, 2,2'-dibromophenyl (DBBP), 2,2'-6,6'-tertbromo-1,1'-biphenyl (TBBP).[23, 63, 99, 100] This infers that full debromination like the molecules in the middle of a unit of three can occur in this experiment as well.

4.1.1.2 Self-assembly *ii*

A high resolution image of self-assembly *ii* reveals that it actually consists of two different self-assemblies which will be called self-assembly ii_α and self-assembly ii_β, see Figure 19a. Self-assembly ii_α is found in small patches at the edges of larger patches of self-assembly ii_β, but never unaccompanied by self-assembly ii_β. Self-assembly
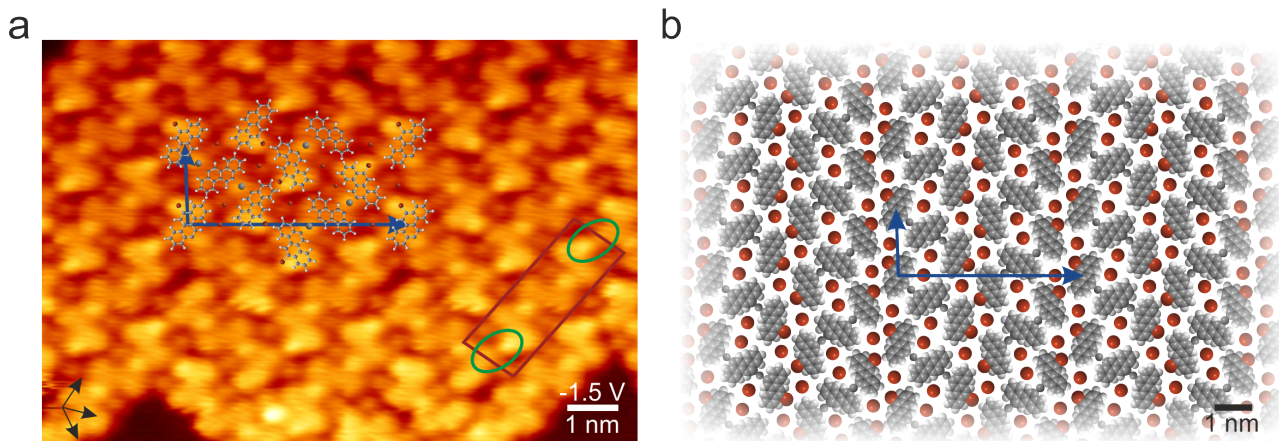
Figure 18: *a) High resolution STM image of self-assembly i including a stick-and-ball overlay of the unit cell. $I = 200pA$, $V = -1.5V$. b) The molecular model of self-assembly i. The unit cell has parameters: $a = 4.36 \pm 0.09nm$, $b = 1.58 \pm 0.07nm$ and $\theta = 91.99 \pm 2.18$.*

ii_β can be found without self-assembly ii_α.

Self-assembly ii_α   Self-assembly ii_α can be seen in the top of Figures 19a and 19b. The self-assembly is resembled by bright bow-tie shaped units, which will be called dashes for now. These dashes change direction every few rows and are separated from each other by small dim dots. The change in direction does not seem to show a particular order. The dashes have a length of approximately 1nm when measured across the long-axis, see the blue line in Figure 19b. This is in reasonable agreement with the length of the carbon backbone of a single DBCh molecule (0.923nm), therefore the long-axis of the dashes is tentatively assigned to the backbone of a DBCh molecule. The change in direction of the dashes is attributed to a difference in chirality of the carbon backbone.

Every one of these dashes is accompanied by two bright dots, giving the bow-tie resemblance. These bright dots can either be the Br atoms of a DBCh molecule or silver adatoms that coordinate with debrominated DBCh molecules. In case the DBCh molecules are intact, the interaction between bow-ties would be halogen bonding (X-bonding). X-bonding in 2D self-assembly typically has a length of 0.3 to 0.5nm, see Refs. [51, 52, 98] for examples of halogen-bonding. The distance between bright protrusions in self-assembly ii_α is 0.72±0.16nm, thus it is unlikely that there is X-bonding between the bright protrusions. Therefore, the bright dots are attributed to silver adatoms that coordinate with the radical sites of debrominated DBCh moleucules. This infers that the dimmer dots, which appear between the bow-tie shaped structures, are the split-off Br atoms. Other examples of split-off halogens that interact with their dehalogenated precursor include Refs. [95–97] Moreover, by assigning the bright dots to silver adatoms and the dimmer dots to Br atoms, the observed contrast is consistent with what was found for self-assembly i and the work of Píš *et al.*[94]

To summarize; the long-axis of the bow-tie shape is attributed to the carbon backbone of a DBCh molecule, the bright dots that accompany these dashes are attributed to silver adatoms that coordinate at the radical sites and the dim dots in between the dashes are attributed to split-off Br atoms. Using this information, a unit cell of the network can be constructed which is depicted in blue in Figure 19a. The unit cell is constructed around carbon backbones that point in the same direction and thus are of the same chirality. The unit cell has parameters $a = 1.24 \pm 0.06nm$, $b = 1.29 \pm 0.1nm$ and $\theta = 60.9 \pm 2.7°$. Because of the bow-tie resemblance of the dashes, this self-assembly will be called the bow-tie network.

Using an overlay of the unit cell, the distance between the split-off Br atoms and the silver adatoms is measured as $0.41 \pm 0.05nm$. This distance is in agreement with the Br-Ag distance of the adatom-coordinated DBA chains in the work of Park *et al.*, which is 0.46±0.02nm.[63] Furthermore, the C-Ag distance is determined as 0.18±0.01nm. This value lies outside the error margin of both the C-Ag distance of the DBA chains (0.23nm) and the DMTP staple shift pattern (0.25nm). The complete debromination of the DBCh molecules is similar to that of DBA, DMTP, DBBP and TBBP on Ag(111), see Section 4.1.1.1.[23, 63, 99, 100] Based on these findings, a molecular model is proposed which can be found in Figure 19c.

Self-assembly ii_β   Self-assembly ii_β can be seen in the bottom of Figures 19a and 19b. It consists of parallel rows. These parallel rows consist of units of two dashes that are connected by one bright dot. The purple box in Figure 19a depicts one of these units of two. The dashes have similar dimensions as the dashes in the

bow-tie network. Therefore, the dashes are again attributed to the carbon backbone of the DBCh molecules. The units of two dashes are separated by two bright dots, of which one is connected to the first unit and the second connected to the following unit. Thus, one unit consists of two dashes and three bright dots. Using the same argument as for the chevron network, the bright dot connecting the two dashes must be a silver adatom. Moreover, this is consistent with the contrast that is seen in the bow-tie network on the same image. Besides, this is consistent with the contrast seen in previous self-assemblies as well as the work of Píš *et al.*[94]

The bright dots at the outsides of a unit of two can be either silver adatoms or the Br atoms of (partially) debrominated DBCh molecules. Every unit of two is surrounded by eight dimmer dots. By considering a second unit next to it, it can be seen that these dimmer dots are shared among units. If we assume the dimmer dots are Br atoms that split-off DBCh molecules, we know that every unit of two should have four whole Br atoms surrounding it. Because the eight dimmer dots are shared with a second unit, it is indeed true that every single unit is surrounded by four whole dimmer dots. Therefore, the dimmer dots are attributed to Br atoms that have split-off from the DBCh molecules. Consequently, the bright dots at the outsides of a unit of two must be silver adatoms that coordinate at the radical sites of the carbon backbone.

With close inspection, it can be seen that not every unit of two dashes has three bright dots. Rather, some units are missing one (or even two) bright dots on the outside. This infers that there is no silver adatom coordinating at that site. Therefore, these defects are attributed to partially debrominated DBCh molecules. This means that there is a C-Br-Ag coordination with the next unit, similar to what is observed in the staple shift pattern in the work of Fan *et al.*[98]

To summarize; the dashes are attributed to the carbon backbone of DBCh molecules, the brighter dots connecting two dashes are attributed to silver adatoms, the dim dots surrounding the units of two are attributed to split-off Br atoms and the bright dots connecting two units of two are attributed to silver adatoms. In case of a missing bright dot, the corresponding dash is considered partially debrominated. With this information, a unit cell can be constructed, which can be seen in purple in Figure 19a. The unit cell has parameters $a = 1.34 \pm 0.09$nm, $b = 12.07 \pm 0.09$nm and $\theta = 104.9 \pm 4.7°$. All molecules in the unit cell are of the same chirality, and the unit cell repeats over long distances. Therefore this network will be called the homochiral network from now on.

Using an overlay on the image in Figure 19a, the bond distances can be determined. The C-Ag-C distance within a unit of two is determined to be 0.49 ± 0.03nm. This in agreement with the two examples of similar coordination of DBA and DMTP mentioned earlier.[63, 98] Furthermore, the distance of the C-Ag coordination at the exterior of a unit of two can be measured using the overlay. This distance is 0.22 ± 0.03nm, which is well in agreement with the distance found in the DBA chains and DMTP staple shift pattern.[63, 98] The Ag-Ag distance between units is 0.39 ± 0.06nm. Meaning their van der Waals radii do not overlap[93]. Lastly, the distance between a split-off Br atom and the closest hydrogen is determined. This distance is 0.33 ± 0.05nm, which is in agreement with the DBA chains found in the work by Park *et al.*[63] Based on these findings, a molecular model is proposed which can be found in Figure 19d.

4.1.1.3 Self-assembly *iii*

The last self-assembly found at room temperature deposition is found along patches of other networks as well as at step edges, see Figure 17. A zoom-in of one of these chains can be seen in Figure 20a. The image shows that the chain consists of dashes that align parallel to each other. The length of one of these dashes is approximately 1nm, thus these are again tentatively assigned to the carbon backbone of DBCh molecules. To understand the coordination between the dashes, we look at the edges of patches of high-resolution images of the other two self-assemblies, for example Figures 18 and 19. These images show that the dashes coordinate together with one bright protrusion in between them and dimmer protrusions next to these bright ones. Similar to the chevron network and the homochiral network, these bright protrusions must be silver adatoms that have diffused from the surface. The silver adatoms coordinate at the radical sites of the debrominated DBCh molecules. In similar fashion, the dimmer dots are assigned to split-off Br atoms.

With this information, an overlay of Figure 20a can be constructed. The first molecule is laid down at the upper end of the chain, which must be a right-handed enantiomer of DBCh in order to be able to coordinate with the next. Using this procedure, the following molecules are laid down resulting in the overlay seen in Figure 20b. Using this overlay, the C-Ag-C length between molecules is determined to be 0.51 ± 0.06nm, which is in agreement with the works of Park *et al.* and Fan *et al.*[63, 98]. Furthermore, the split-off Br atoms coordinate in a similar fashion to the DBA chains in the work of Park *et al.*[63]. Therefore, the overlay uses the distance measured by Park *et al.*, which is 0.46 ± 0.02nm. Based on these findings, a molecular model is proposed which can be seen in Figure 20c. Because the chains consist of both chiralities, self-assembly *iii* will be called heterochiral chains from now on.
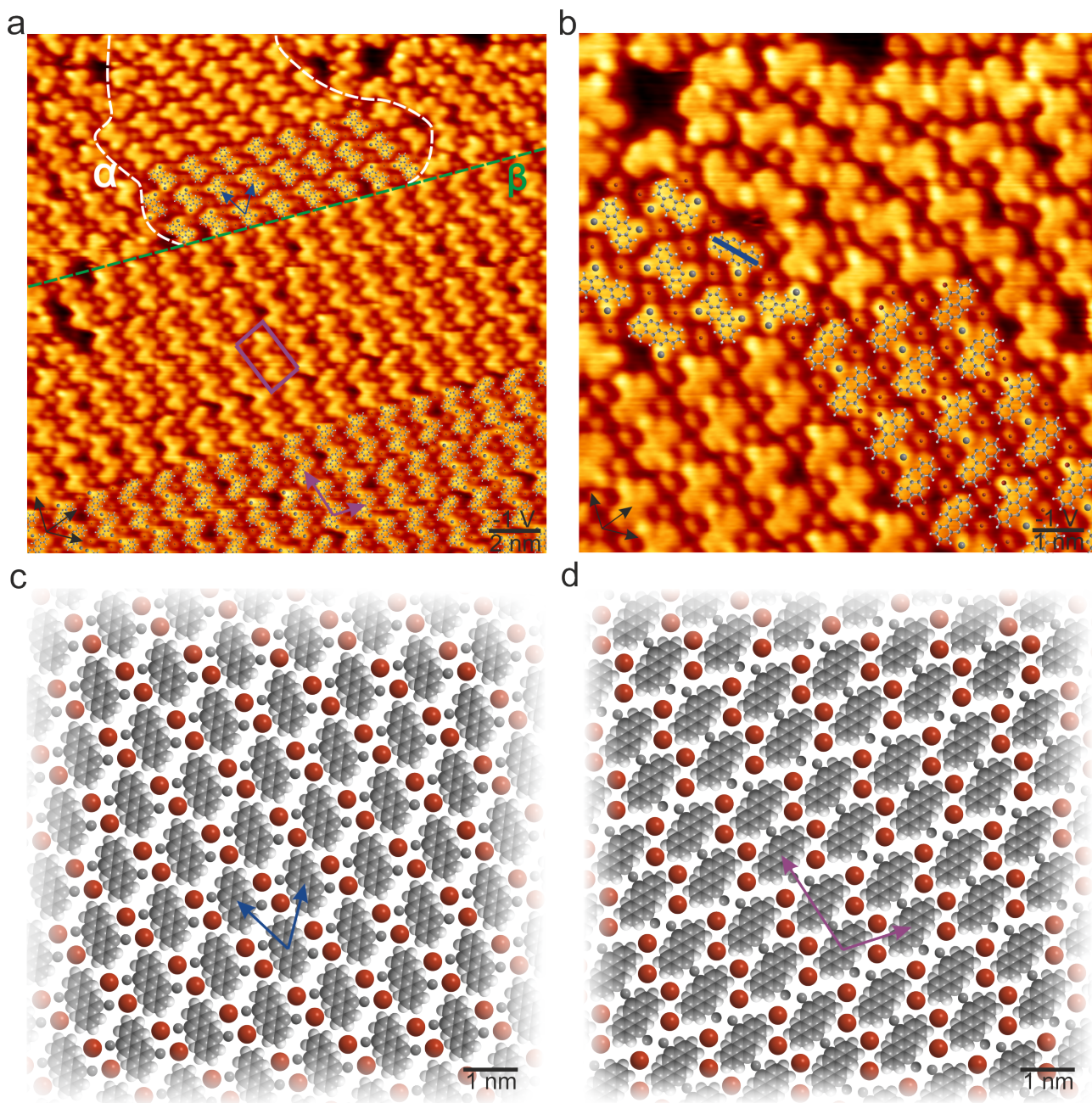
Figure 19: *a) High resolution STM image of a self-assembly ii, which shows self-assemblies ii_α (top) and ii_β (bottom) in an overlay. The blue arrows indicate the unit cell directions of self-assembly ii_α. The purple box depicts a unit of two of self-assembly ii_β, the purple arrows indicate the unit cell directions. $I = 200pA$, $V = -1V$. b) High resolution STM image showing self-assembly ii in more detail. The blue line indicated the direction of the long axis of one dash. $I = 200pA$, $V = -1V$. c) The molecular model of self-assembly ii_α. The unit cell has parameters $a = 1.24 \pm 0.06nm$, $b = 1.29 \pm 0.1nm$ and $\theta = 60.9 \pm 2.7°$. d) The molecular model of self-assembly ii_β. The unit cell has parameters $a = 1.34 \pm 0.09nm$, $b = 12.07 \pm 0.09nm$ and $\theta = 104.9 \pm 4.7°$.*
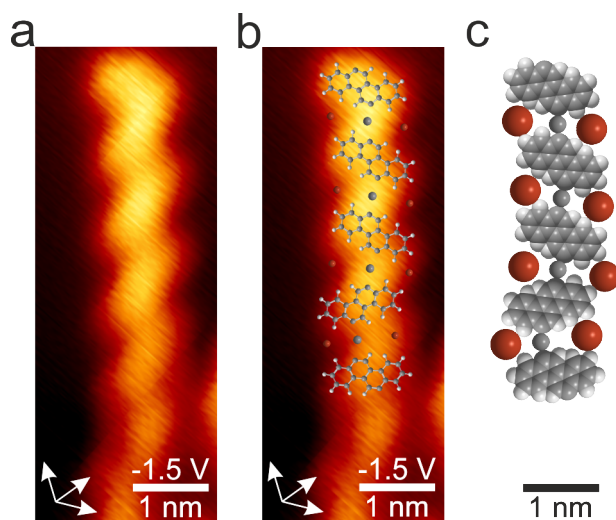
Figure 20: *a) Zoom-in of self-assembly iii found at room temperature deposition. $I = 20pA$, $V = -1.5V$. b) Same as a) but with superimposed molecules. $I = 20pA$, $V = -1.5V$. c) The tentative molecular model over self-assembly iii. No unit cell is determined because of the randomness of the chiralities.*

4.1.2 Deposition at elevated temperatures

4.1.2.1 Deposition at 100°C

In the following experiment the Ag(111) substrate was kept at 100°C during deposition to increase the kinetic energy of the molecules as they reach the surface. This resulted in large islands of parallel rows, which will be called self-assembly j and can be seen in Figure 21. Self-assemblies i, ii and iii are no longer found. The islands stretch as far as 80nm and are found in six different directions. Interestingly, deposition at 120°C leads to similar islands in looks but are even larger ($> 120nm^2$).

A close-up image of the network (Figure 22a) reveals that it consists of dashes and both bright and dim dots. The dashes are connected by only one bright dot. The dashes have similar dimensions as the ones on previous samples and are therefore tentatively assigned to the carbon backbone of a DBCh molecule. As there is only one bright protrusion between every dash, the bright protrusions must be silver adatoms. Following similar arguments as before, every dash is accompanied by two bright protrusions, inferring it coordinates with two silver adatoms. This infers the molecules are fully debrominated. In turn, this infers that the dimmer dots, which appear along the rows, are Br atoms that have split-off the DBCh molecules. The number of dim dots found along the rows confirm this suspicion. Other examples of split-off halogens that coordinate with their dehalogenated precursor include Refs. [95–97] Furthermore, by viewing how the silver adatoms coordinate with the carbon backbone, the chirality of the molecule can be determined. It can be seen that the chiralities do not alternate the left- and right-handed enantiomers every row but rather there are some defects, see for example the blue box in Figure 22a where two left-handed enantiomers coordinate together.

Using this information, an overlay can be constructed on the image, see Figure 22b. Using the overlay the C-Ag-C distance is determined as 0.51 ± 0.03nm. This is agreement with other networks and the works of Park *et al.* and Fan *et al.*[63, 98] Furthermore, the Ag-Br distance can be determined. This distance is 0.50 ± 0.09nm, which is in agreement with the Br-Ag distance determined for self-assembly ii_α and the distance in the DBA chains in the work of Park *et al.*[63] The large uncertainty is due to some Br atoms that lie around defects. By considering the case where the left- and right-handed enantiomers are alternated, a molecular model can be constructed from the determined distances. This model is given in Figure 22b. The unit cell of the ideal case has parameters $a = 1.44$nm, $b = 1.78$nm and $\theta = 77.4°$. This is in accordance with what is measured on the overlay in an ideal part. Self-assembly j will now be called networks of heterochiral chains. The chains are similar to what was found in the work of Nyendaal whom deposited the same precursor molecule on Ag(110).[2] However, in the case of Ag(110), large islands of heterochiral chains are formed upon deposition at room temperature, but homochiral chains are formed upon deposition at 100°C.

To understand how the networks of heterochiral chains align along the principal directions of the Ag(111) surface, LEED measurements were taken. To create sufficiently large patches molecules were deposited on a sample kept at 120°C. Deposition at this temperature leads to similar networks as deposition at 100°C but with larger islands, thus more suitable for LEED.

The principal directions of the Ag(111) surface were determined at an electron energy of 100.4eV. By determining the vector between the (0,0)-spot and a surface spot the angle of the network in relation with the principal directions can be determined. The LEED pattern of the network was taken at an electron energy
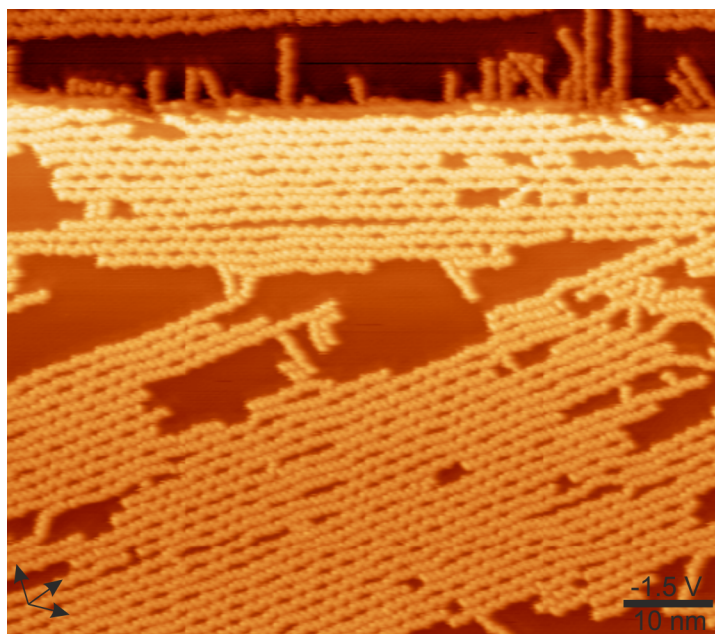
Figure 21: *An overview STM image of self-assembly j found when depositing DBCh on Ag(111) kept at 100°C,*
I = 20pA, V = −1.5V.

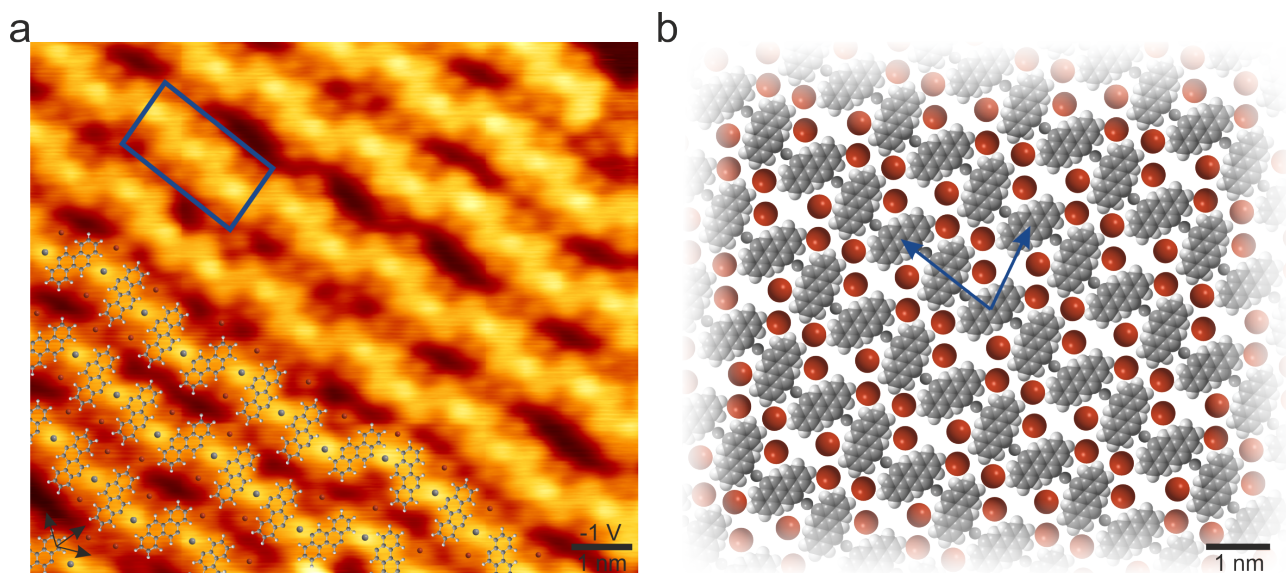***Figure 22:*** *a) An overview STM image of self-assembly j found when depositing DBCh on Ag(111) kept*
at 100°C. I = 20pA, V = −1V. b) The molecular model of self-assembly j. The unit cell has parameters
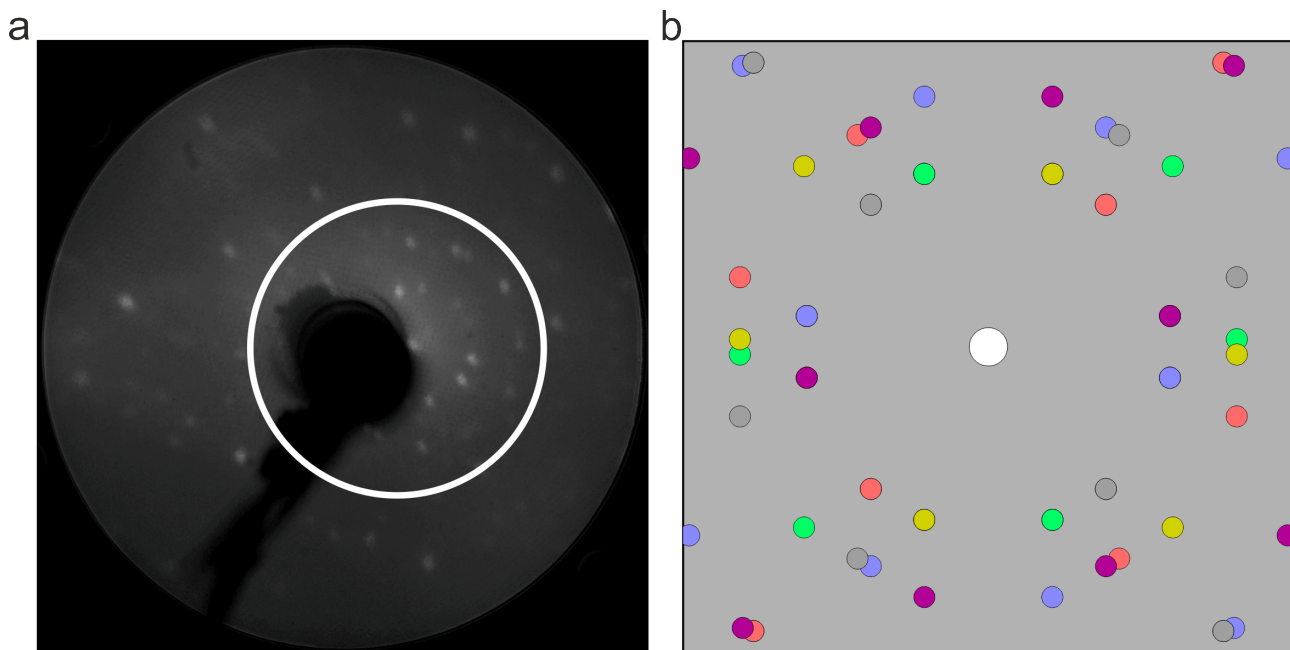*a = 1.44nm, b = 1.78nm and θ = 77.4°.*

Figure 23: *a) The LEED-pattern showing the network spots taken at 29.9eV. The (0,0)-spot is slightly to the right of the electron gun. b) Simulation of the network LEED-pattern. The (0,0)-spot is shown in white, every color depicts one domain. Only the area indicated within the circle in a) is shown.*

of 29.9eV and can be seen in Figure 23a. The surface spots from the Ag(111) surface are similar to what is expected from theory on LEED (see Section 3.3) and can be seen in Figure 31 in Appendix B. The angle is found to be 14°, and is used to simulate the LEED-pattern in Figure 23b. The LEED-pattern and the simulated LEED-pattern agree well. Thus, it is concluded that the network of heterochiral chains align with a 14° shift along the principal directions. STM images show that indeed the networks are found in six distinct directions.

4.1.2.2 Deposition at 150°C

Deposition of DBCh on Ag(111) kept at 150°C led to the formation of small islands of chains that align parallel to each other, see Figures 24a and 24b. The difference between these samples will be made clear below. The self-assemblies can be seen in more detail in Figure 25.

The self-assemblies consists of dashes and bright dots. The dashes have similar dimensions to those in previous self-assemblies (1nm) and are therefore tentatively assigned to the carbon backbone of a DBCh molecule. The dashes are connected by only one bright dot. Similarly to previous self-assemblies, the bright protrusions are attributed to silver adatoms. This infers that the DBCh molecules have fully debrominated, even though the Br atoms cannot be seen in the images. This could be due to the polarity of the bias. The Br atoms can only be seen at a negative bias voltage, see the previous sections. Furthermore, by checking how the silver adatoms coordinate with the carbon backbone, the chirality of the molecule can be determined. It can be seen that the left- and right-handed enantiomers do not alternate. Rather there are some defects where a molecule coordinates with a molecule of the same chirality.

Deposition of DBCh on Ag(111) kept at 150°C with a similar deposition rate (0.09ML/min) as previously discussed samples led to the formation of smaller islands of chains than with a higher deposition rate, see Figure 24a. By increasing the deposition rate to 0.3ML/min but adjusting the time so that the coverage should be similar, the islands became larger, see Figure 24b. High-resolution images of both self-assemblies (Figure 25) reveal that the islands are similarly coordinated. The difference in coverage could be related to the difference in kinetic energy of the molecules that land on the surface. A higher deposition rate gives the molecules a higher kinetic energy, which allows the molecules to diffuse across the surface. It could be that the kinetic energy of the sample with low deposition rate is too low for the molecules to find each other, leading to desorption of the molecules.

With this information, an overlay can be constructed for both images, see Figure 25. The split-off Br atoms are given the same distance as in self-assembly *j*, which is based on the distance of the work of Park *et al.*[63] Using the overlay, the C-Ag-C distance is determined as 0.52 ± 0.04nm and 0.49 ± 0.05nm for low deposition and high deposition samples, respectively. This is in accordance with the works of Park *et al.* and Fan *et al.*[63, 98] Moreover, the self-assemblies have similar distances for both low and high deposition, as well as self-assembly *j*. This infers the self-assemblies are the same, albeit that at deposition at 150°C leads to smaller islands.
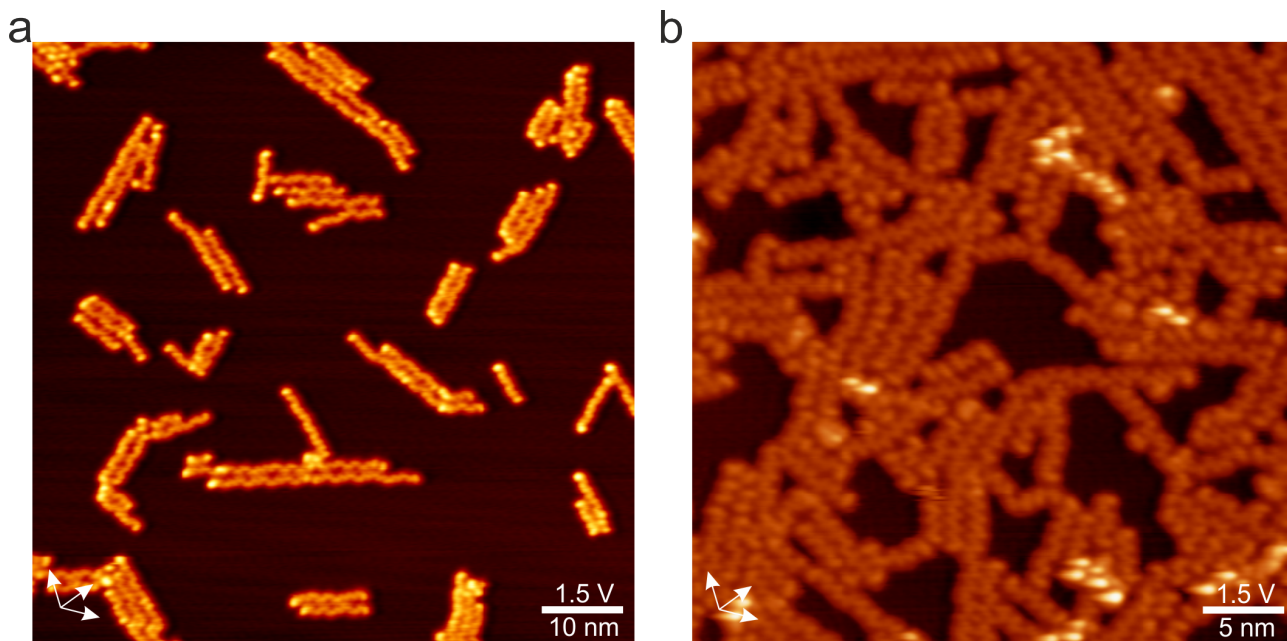
Figure 24: *a) Overview STM image of a sample that was kept at 150°C during deposition with a low deposition rate (deposition rate 0.09ML/min, coverage 0.36ML). I = 20pA, V = 1.5V. b) Overview STM image of a sample that was kept at 150°C during deposition with a high deposition rate (deposition rate 0.3ML/min, coverage 0.72ML). I = 20pA, V = 1.5V.*

Therefore, the same molecular model as the networks of heterochiral chains is proposed, see Figure 22b.

With close inspection it can be seen that the left- and right-handed enantiomers alternate in both samples. See for example Figures 26a and 26b and a molecular model of this chain in Figure 26c. By counting the number of possible alternations and the number of alternations that happen within a chain it can be determined if the chain is alternating due to chance or because this is the preferred coupling scheme. This is done using the following procedure: *i*) the sequence of a chain is written down, for example the lower chain in Figure 26a has the sequence 'RLRRLRLRRLRL'. *ii*) The number of possible alternations $n-1$ is determined, where n is the chain length, in this case 11. *iii*) The number of alternations in the chain is determined, in this case nine. *iv*) Using a binomial distribution,

$$P(k) = \binom{n}{k} p^k (1-p)^{n-k} \tag{31}$$

which is essentially a coin flip, the probability of the alternations in this chain being random can be calculated.

This procedure is done for both the low- and high-deposition rate samples using high-resolution images. In case of low deposition rate, there were 87 possible alternations. The left- and right-handed enantiomers were alternated 70 times. Using Equation 31 it is determined that the probability of this number of alternations being random is $4 \cdot 10^{-9}$. In case of higher deposition rate, there were 157 possible alternations and 119 alternations happened. The probability of this number of alternations being random is $3 \cdot 10^{-11}$. The extremely low probability infers that the left- and right-handed enantiomers are alternated because this is the preferred coupling scheme.

4.1.3 Post-deposition annealing at elevated temperatures

4.1.3.1 Annealing to 90°C

To understand the influence of temperature in more detail, samples that were deposited at room temperature were annealed to 90°C post-deposition. This led to the formation of islands of rows that align parallel to each other, which will be called self-assembly l, see Figure 27a.

A close-up image of self-assembly l reveals that it consists of dashes and both bright and dim dots, see Figure 27b. The dashes are connected by one bright dot, meaning it has to be a silver adatom, similar to self-assemblies j and k. The dashes are of the same dimension as previous self-assemblies and are thus attributed to the backbone of fully debrominated DBCh molecules. The dim dots are attributed to split-off Br atoms. The number of dim dots found along the rows confirm that the DBCh molecules are fully debrominated. The chirality of the backbone can be determined by viewing how the silver adatoms coordinate with a dash. It can be seen that the left- and right-handed enantiomers are not alternated. Instead, it seems that the chains consists of random chiralities.
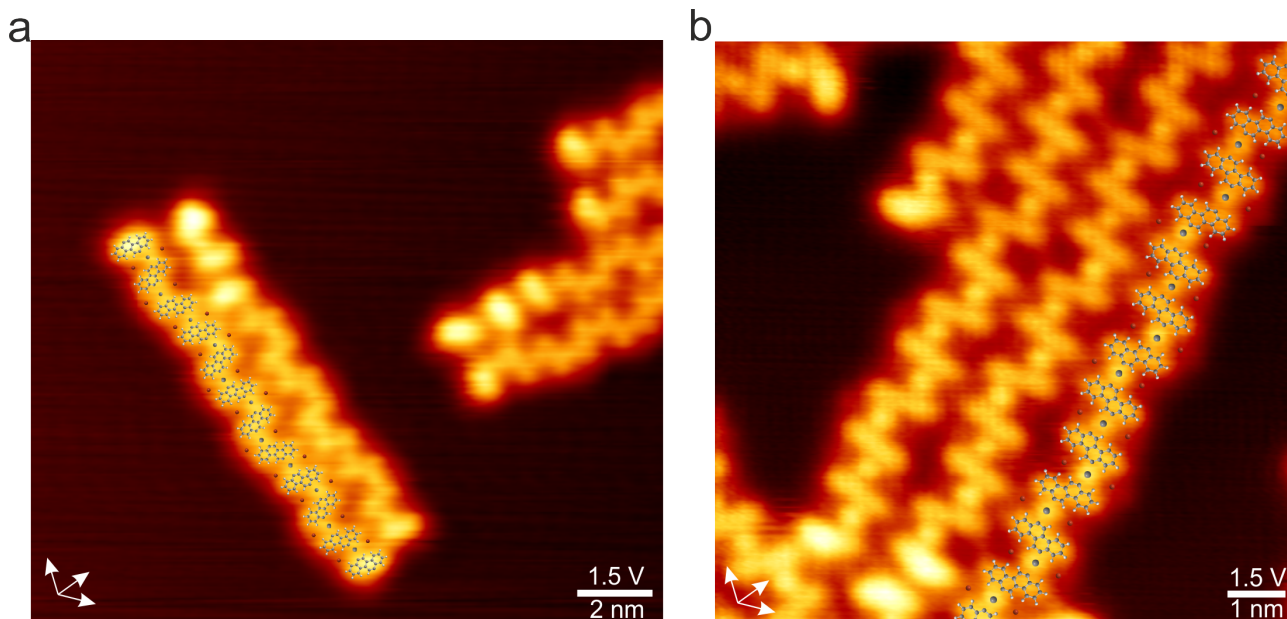
Figure 25: *a) High resolution STM image of self-assembly k found when depositing DBCh on Ag(111) kept at 150°C with a low deposition rate. I = 20pA, V = 1.5V. b) High resolution STM image of self-assembly k found when depositing DBCh on Ag(111) kept at 150°C with a high deposition rate. I = 50pA, V = 1.5V.*
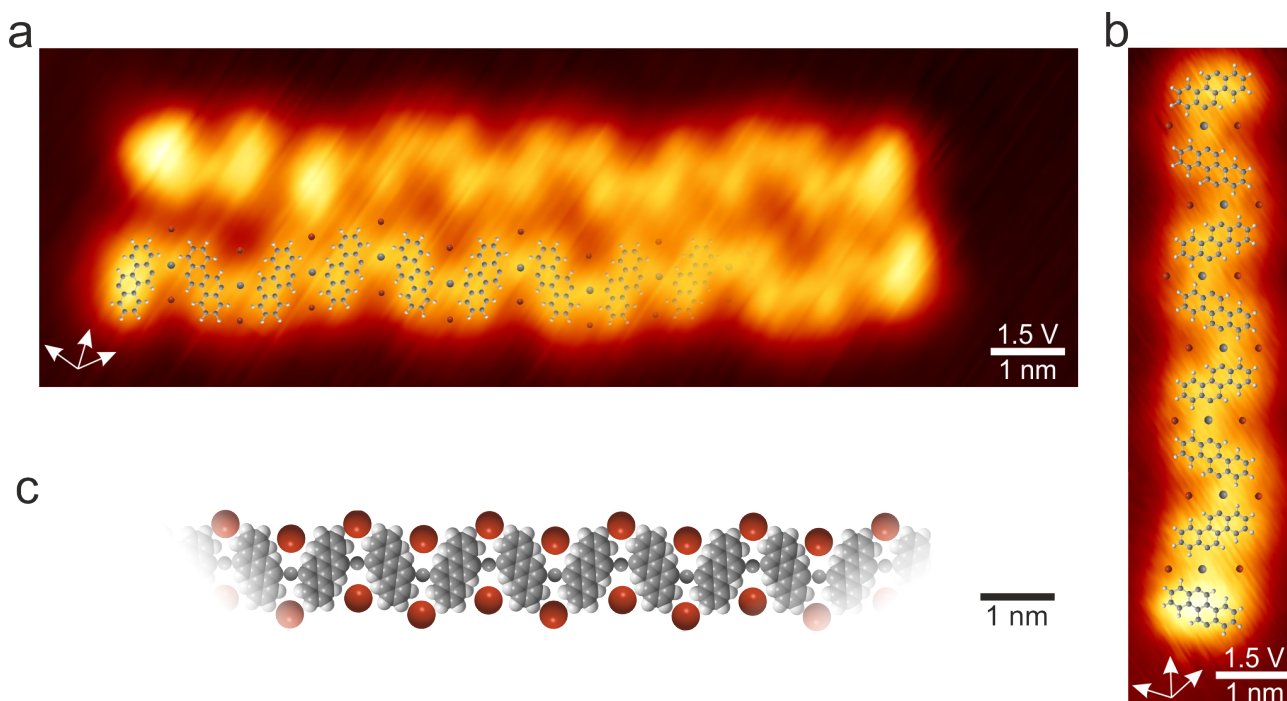
Figure 26: *a) High resolution image of self-assembly k found when depositing DBCh on Ag(111) kept at 150°C with a low deposition rate. The chain that has an overlay alternates the left- and right-handed enantiomers of DBCh. I = 20pA, V = 1.5V. b) High resolution image of a single chain on the same sample including an overlay. The left- and right-handed enantiomers alternate like in a chevron-like GNR. I = 20pA, V = 1.5V. c) Molecular model of a chain that alternates the left- and right-handed enantiomers.*

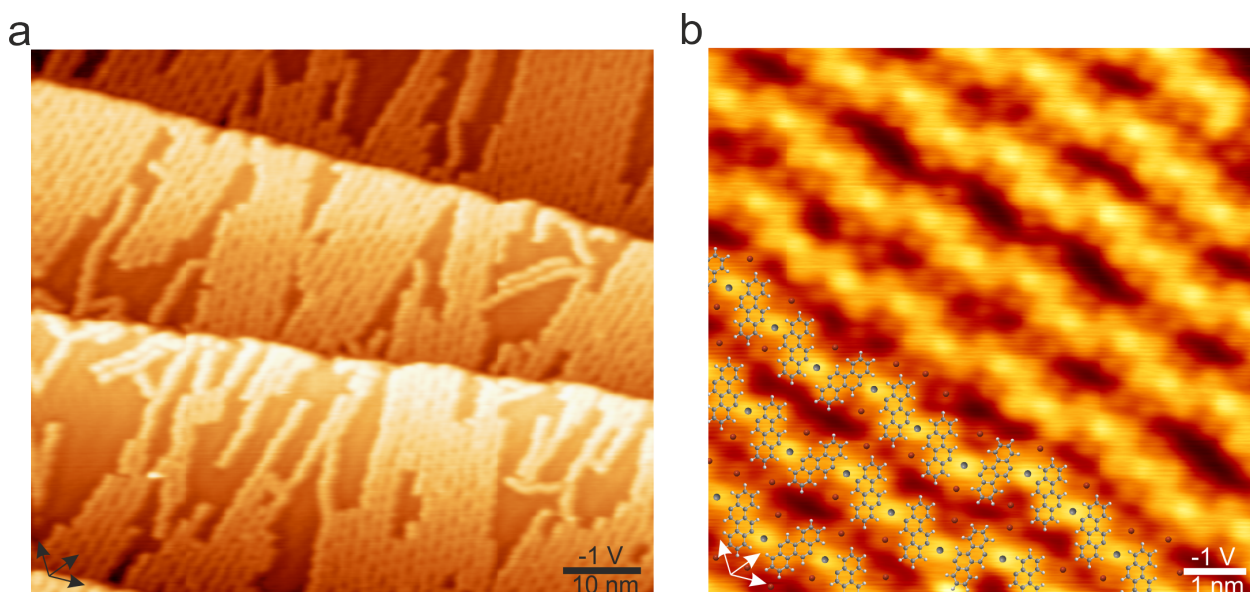**Figure 27:** *a) An overview STM image of self-assembly l found when depositing DBCh on Ag(111) kept at RT and subsequently annealed to 90°C. $I = 20pA$, $V = -1V$. b) High resolution STM image of self-assembly l with an overlay. $I = 200pA$, $V = -1V$.*

Using this information, an overlay can be constructed on the image in Figure 27b. The C-Ag-C distance is determined from this overlay as 0.49 ± 0.04nm, which is in agreement with the works of Park *et al.* and Fan *et al.*[63, 98] Furthermore, the Br-Ag distance can be determined. This distance is 0.49 ± 0.07nm, which is in agreement with the distance found in the chains of DBA molecules.[63] Because of the randomness of the chiralities no molecular model is suggested.

4.1.3.2 Annealing to 150°C

In the following experiment the sample was annealed to 150°C post-deposition. This resulted in chains and small networks of chains as can be seen in the overview image in Figure 28a, which will be called self-assembly *m*. High resolution images of the chains and the networks reveal that they are similarly coordinated, see Figures 28b and 28c. Both consist of dashes and both bright and dimmer dots. The dashes have similar dimensions to those in previous samples and are therefore assigned to the carbon backbone of a DBCh molecule. The dashes are connected by a single bright dot, meaning the DBCh molecules are fully debrominated. The dim dots that sit at the sides of the chain and within the network are assigned to the split-off Br atoms. The chirality of the carbon backbone can be determined from the way it coordinates with the silver adatoms. There is no clear order in which the chiralities appear in both the network and the chains.

Using this information, an overlay can be constructed for both the chain and the network. Using the overlay, the C-Ag-C distance of the chain is determined as 0.51 ± 0.04nm. This is in agreement with the values found in previous networks and literature.[63, 98] The C-Ag-C distance in the network is determined as 0.54 ± 0.05nm, which is also in agreement with these works.[63, 98] Furthermore, the Ag-Br distance is determined as 0.52 ± 0.05nm and 0.54 ± 0.08nm for the chains and network, respectively. Both distances are in agreement with previous self-assemblies and the distance measured in the work of Park *et al.*[63] Because of the randomness of the chiralities, no molecular model is proposed. However, regarding the distances the models of the heterochiral chain in Figure 20c and the network of heterochiral chains in Figure 22b would work.

4.1.3.3 Annealing to 160°C

The sample that was deposited at 150°C showed that with a low deposition rate it is possible to alternate the left- and right-handed enantiomers within a chain. In order to synthesize a GNR from this polymer annealing at a higher temperature is needed. Therefore, the previous sample was subsequently annealed to 160°C with the goal of synthesizing GNRs. The STM images in Figures 29 show that the molecules clumped together with no particular order. This is similar to what is seen on Ag(110) in the work of Nyendaal [2]. DBCh was deposited on Ag(110) at room temperature, this sample was subsequently annealed to 150°C which resulted in similar clumps of molecules. The image in Figure 29a shows dim dots all around the clumps. These dim dots are hard to see in the image 29b, however in this image bright dots between dashes can be seen more clearly. In similar fashion as previous samples, the bright dots are attributed to silver adatoms and the dim dots are attributed to split-off Br atoms. No molecular model is proposed because of the lack of order.
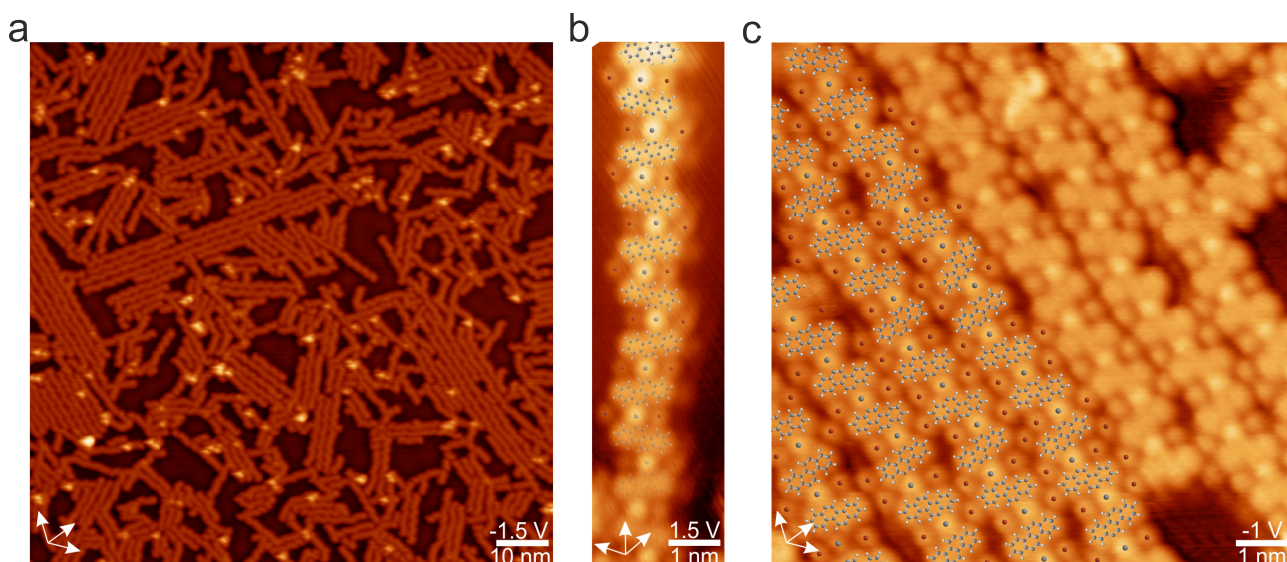
Figure 28: *a) Overview STM image of self-assembly m that was annealed around 150°C post-deposition. The image shows single chains and small networks of chains. $I = 20pA$, $V = -1.5V$. b) High resolution STM image of one such chain, including an overlay. $I = 50pA$, $V = 1.5V$. c) High resolution STM image of one such network. $I = 50pA$, $V = -1V$.*
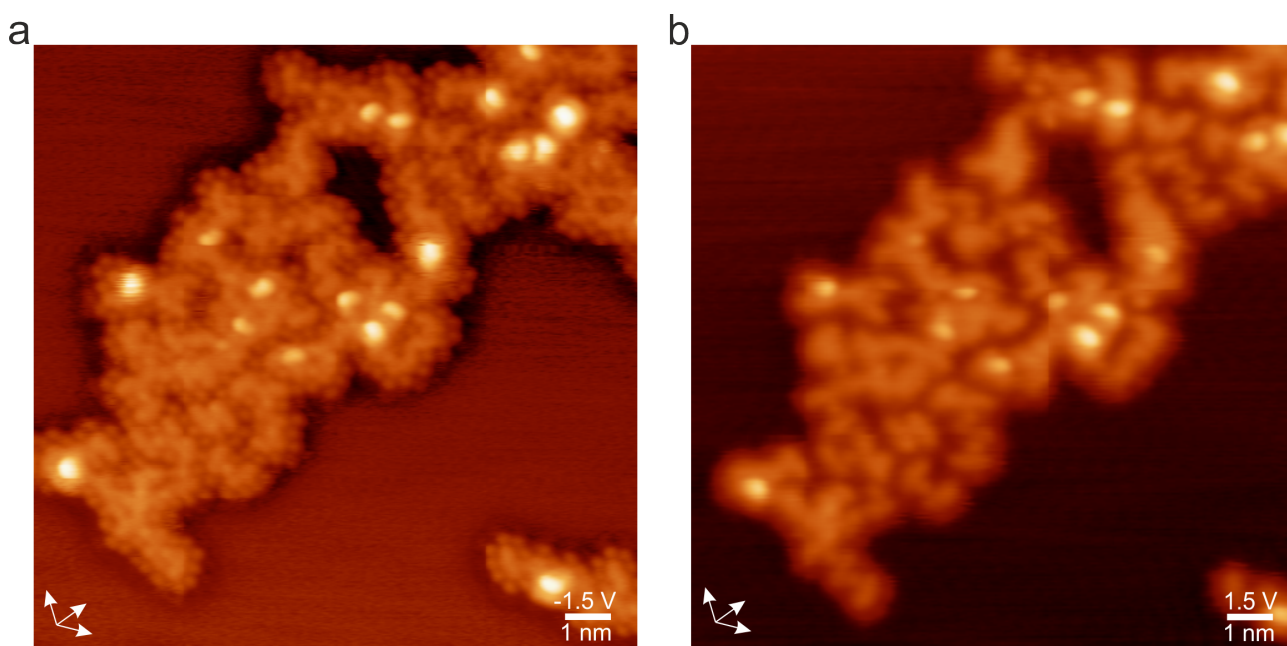
Figure 29: *a) High resolution STM image of the molecular clumps seen after annealing above 160°C. The dots surrounding the molecules are Br atoms. $I = 20pA$, $V = -1.5V$. b) STM image of the molecular clumps taken at a positive bias voltage. The Br atoms can no longer be seen individually, however, the silver adatoms between molecules are more clear. $I = 20pA$, , $V = 1.5V$.*

5 Discussion

The goal of this study was to synthesize chevron-like GNRs on Ag(111) from the molecular precursor DBCh. It is clear that it is not possible to synthesize these GNRs via thermally induced Ullman-type coupling and subsequent cyclodehydrogenation. Previous work of Pham *et al.* theorised that GNRs could not be formed on Cu(111) due to chiral-selectivity.[1] On Cu(111) homochiral metal-coordinated chains (Figure 6c) were formed which could not be transformed to GNRs upon further annealing. In this work, we were able to synthesize chains that alternated the left- and right-handed enantiomers -similar to the polymer intermediate obtained by Pham *et al.*[1] on Au(111)- by depositing on a sample kept at 150°C. Upon annealing these chains, disordered islands of molecules were found, see for example Figure 29. Therefore, it is concluded that the chiral-selectivity is not the main reason that GNRs could not be synthesized on this substrate. Rather, it is thought that the metal-coordination prevents the synthesis of GNRs. The silver adatoms that coordinate at the radical sites of the DBCh molecules were not removed even upon annealing to 300°C. This indicates that the silver adatoms coordinate strongly with the carbon backbone of the DBCh molecules. The coordination of a silver adatom at the radical sites prevents the enantiomers from covalently linking to form a chevron-like GNR.

It should be noted that it is possible to transform metal-organic hybrids to GNRs, as was first shown by Zhang *et al* in 2015.[101] Similarly, Sun *et al.* showed the synthesis of a 5-AGNR from a metal-organic intermediate on Ag(111).[102] This could indicate that not only the metal-coordination is preventing the synthesis of GNRs but steric hindrance might play a role as well. A metal-organic bond is 0.2-0.3nm longer than a carbon-carbon bond, thus keeping the monomers further apart.[68] If the silver adatom is removed, the bond is shortened leading to steric hindrance between the hydrogens of the covalently linked monomers. Consequently, the polymer does not lie plane on the substrate anymore, like for example the polymer intermediate found by Pham *et al.*[1] It would cost additional energy to planarize the polymer intermediate before forming a GNR.

Interestingly, it was observed that a small difference in temperature changes the (sizes of) self-assemblies drastically. Deposition at 25°C led to the formation of the chevron network, the bow-tie network, the homochiral network and heterochiral chains. Whereas, deposition at 31 or 33°C formed only the chevron network and the heterochiral chains. Moreover, the patches of the chevron network were smaller at these slightly higher temperatures. Similarly, a ten degree difference in post-deposition annealing temperatures led to completely different self-assemblies. Annealing to 150°C led to the formation of (networks of) heterochiral chains, whereas annealing to 160°C led to the formation of disorded clumps of molecules. This shows that the self-assemblies found on Ag(111) are sensitive to a small chance in temperature.

The different coordination lengths for different self-assemblies are summarized in Figure 30. Figure 30a shows that the measured C-Ag-C distance is in accordance with the works of Park *et al.* and Fan *et al.* for all self-assemblies that had this kind of coordination.[63, 98] The C-Ag distance of self-assembly ii_α does not agree with these works.[63, 98] Still, a model with C-Ag coordination is suggested because a halogen-bonded network was not possible as the distance between halogens was too large for an attractive interaction. Figure 30c shows that the Br-Ag distance is in accordance with the distance found in the DBA chains in the work of Park *et al.*[63] Lastly, the Br-H distance of the chevron network is not in accordance with literature. One reason for this could be that in this network the Br in question is still attached to a molecule, rather than split-off like in the DBA chains [63] and the homochiral network. The coordination lengths were determined using overlays on (high-resolution) images. It should be noted that this was often done for only one image.

In order to conclude with certainty on the partial debromination seen in the chevron network XPS measurements need to be done. However, as the DBCh molecules self-assemble into three distinct self-assemblies upon deposition at room temperarute this is not possible. To do this, in a future experiment it is suggested to cool a sample before deposition in hopes that the molecules do not debrominate and self-assemble into only one network.

The Br atoms that split-off the DBCh molecules were observed even at samples that were annealed to 160°C, see Figure 29a. This indicates the Br atoms do not desorb on the investigated temperatures. Píš *et al.* investigated the desorption of split-off Br atoms and concluded that they do not desorb from the surface until a temperature of 573K is reached.[94] In this thesis no samples that were annealed to (or above) 573K were not investigated and therefore it is concluded that the split-off Br atoms have not desorbed from the surface on any of the investigated samples.

In previous works it was shown that DBCh can form GNRs on Au(111)[1, 69], forms homochiral polymers on Cu(111)[1] and its chiral-selectivity can be controlled with temperature on Ag(110)[2]. This work gives more insight into the influence of the substrate. It shows that by controlling the temperature during deposition or by annealing post-deposition, different self-assemblies of DBCh can be formed on Ag(111). However, no GNRs were synthesized. Future studies on this precursor molecule could give a broader understanding on the influence of the substrate by using for example Au(110) as a substrate. This would give more insight on the influence of the material of a substrate rather than its crystal structure and could potentially lead the a better understanding on why GNRs are formed or not.
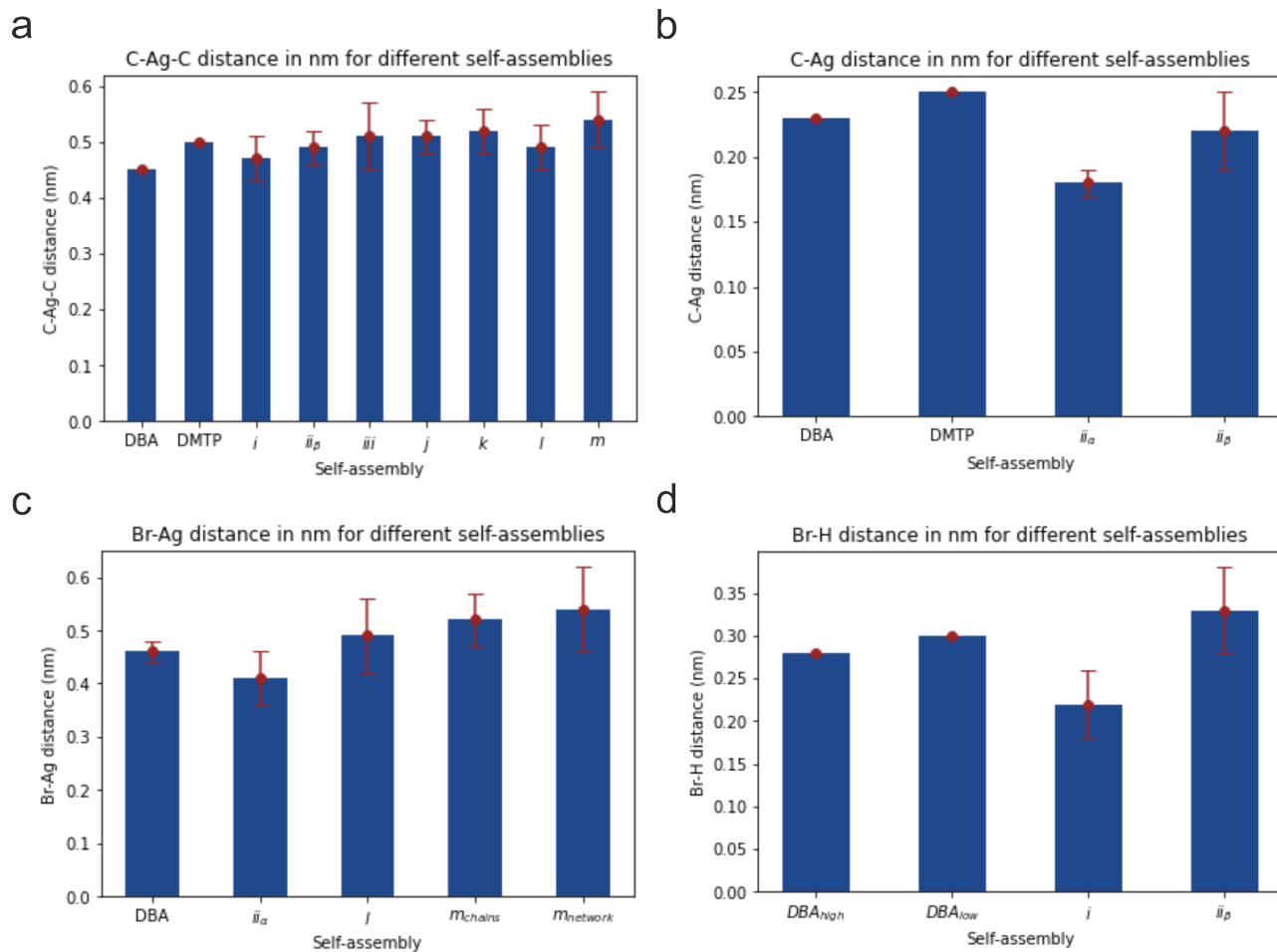
a

b

c

d

Figure 30: *a) The C-Ag-C distance of different self-assemblies on Ag(111) from this thesis and other works.[63, 98] b) The C-Ag distance[63, 98]. c) The Br-Ag distance[63, 98]. d) The Br-H distance[63].*

6 Conclusion

In this work, the on-surface polymerization of the prochiral molecule 6,12-dibromochrysene on Ag(111) was studied. Upon deposition at room temperature four different self-assemblies were found, the chevron network, the bow-tie network, the homochiral network and heterochiral chains. The chevron network consists of both fully debrominated DBCh molecules as well as partially debrominated DBCh molecules. These coordinate to each other via a silver adatom. The bow-tie network consists of fully debrominated DBCh molecules that coordinate with two silver adatoms that coordinate at the radical sites of the carbon backbone of a DBCh molecule. The homochiral network consists mainly of fully debrominated DBCh molecules that coordinate in pairs. The molecules within a pair coordinate together via a silver adatom. The last self-assembly that was found with deposition at room temperature was the heterochiral chains. The molecules in these chains coordinated together via a silver adatom. These chains showed no order in which the left- and right-handed enantiomers coordinate together.

Upon deposition at elevated temperatures heterochiral chains and networks of these chains were formed. Upon deposition at 100°C only networks of these chains were found, whereas upon deposition at 150°C also single chains were found. These chains were similarly coordinated, in both cases the molecules coordinated with a silver adatoms at the radical site. Deposition at 150°C led to chains that alternate the left- and right-handed enantiomer of DBCh. Upon annealing these chains further no GNRs were formed. In contrast to earlier work on this precursor molecule[1, 2], it is concluded that the chiral-selectivity is not the reason no GNRs are formed. Rather, the coordination of a silver adatom at the radical sites means the enantiomers cannot covalently link upon further annealing.

Post-deposition annealing to 90°C at different temperatures transformed all self-assemblies to networks of heterochiral chains. The heterochiral chains were similar to the chains found upon deposition at 100°C and 150°C and are metal-coordinated. Further annealing to 150°C led to the breaking up of these networks. Only small networks and shorter chains were found. These chains had similar coordination. Annealing to 160°C broke these chains and led to the formation of disorded clumps. It is concluded that with post-deposition annealing none of the self-assemblies that were investigated can be transformed to GNRs.

Future studies on this precursor molecule could give a broader understanding on the influence of the substrate by using for example Au(110) as a substrate. This would give more insight on the influence of the material of a substrate rather than its crystal structure and could potentially lead the a better understanding on why GNRs are formed or not. A better understanding on the formation of GNRs could ultimately lead to easier synthesization that could make GNRs even more interesting as the next candidate for silicon-based electronics.

References

[1] T Pham et al. "Chiral-Selective Formation of 1D Polymers Based on Ullmann-Type Coupling: The Role of the Metallic Substrate". In: *Small* 13.13 (2017), p. 1603675.

[2] F Nyendaal. "On-surface polymerization of 6, 12-dibromochrysene on Ag (110)". MA thesis. University of Groningen, 2020.

[3] B Swanson. *Apollo 11, mankind, and Moore's law.* 2019. URL: https://www.aei.org/technology-and-innovation/apollo-11-mankind-and-moores-law/ (visited on 03/09/2022).

[4] J Tomayko. "Computers in spaceflight: The NASA experience". In: *Kent, Allen; Williams, James G., eds. Encyclopedia of Computer Science and Technology* 18.NAS 1.26: 182505 (1988).

[5] Wikimedia Foundation Inc. *Apollo Guidance Computer — Wikipedia, The Free Encyclopedia.* [Online; accessed 17-March-2022]. 2022. URL: https://en.wikipedia.org/w/index.php?title=Apollo_Guidance_Computer&oldid=1068527888.

[6] B Swanson. *The A12 chip: Estimating innovation with Iphone prices.* 2018. URL: https://www.aei.org/technology-and-innovation/the-a12-chip-estimating-innovation-with-iphone-prices/ (visited on 03/09/2022).

[7] Wikimedia Foundation Inc. *Iphone XS — Wikipedia, The Free Encyclopedia.* [Online; accessed 17-March-2022]. 2021. URL: https://en.wikipedia.org/w/index.php?title=IPhone_XS&oldid=1076002867.

[8] Gordon E Moore. "Cramming more components onto integrated circuits, Reprinted from Electronics, volume 38, number 8, April 19, 1965, pp. 114 ff." In: *IEEE solid-state circuits society newsletter* 11.3 (2006), pp. 33–35.

[9] L Grill et al. "Nano-architectures by covalent assembly of molecular building blocks". In: *Nature Nanotechnology* 2.11 (2007), pp. 687–691.

[10] K Novoselov et al. "Electric field effect in atomically thin carbon films". In: *Science* 306.5696 (2004), pp. 666–669.

[11] F Schwierz. "Graphene transistors". In: *Nature Nanotechnology* 5.7 (2010), pp. 487–496.

[12] K Nakada et al. "Edge state in graphene ribbons: Nanometer size effect and edge shape dependence". In: *Physical Review B* 54.24 (1996), p. 17954.

[13] Y Son et al. "Energy gaps in graphene nanoribbons". In: *Physical Review Letters* 97.21 (2006), p. 216803.

[14] J Feng et al. "How size, edge shape, functional groups and embeddedness influence the electronic structure and partial optical properties of graphene nanoribbons". In: *Physical Chemistry Chemical Physics* 23.36 (2021), pp. 20695–20701.

[15] J Cai et al. "Atomically precise bottom-up fabrication of graphene nanoribbons". In: *Nature* 466.7305 (2010), pp. 470–473.

[16] Z Fei et al. "Edge and surface plasmons in graphene nanoribbons". In: *Nano Letters* 15.12 (2015), pp. 8271–8276.

[17] D Wei et al. "Controllable unzipping for intramolecular junctions of graphene nanoribbons and single-walled carbon nanotubes". In: *Nature Communications* 4.1 (2013), pp. 1–9.

[18] L Jiao et al. "Facile synthesis of high-quality graphene nanoribbons". In: *Nature Nanotechnology* 5.5 (2010), pp. 321–325.

[19] J Laskin et al. "Soft landing of complex ions for studies in catalysis and energy storage". In: *The Journal of Physical Chemistry C* 120.41 (2016), pp. 23305–23322.

[20] F Schulz et al. "Precursor geometry determines the growth mechanism in graphene nanoribbons". In: *The Journal of Physical Chemistry C* 121.5 (2017), pp. 2896–2904.

[21] A Kimouche et al. "Ultra-narrow metallic armchair graphene nanoribbons". In: *Nature Communications* 6.1 (2015), pp. 1–6.

[22] L Talirz et al. "On-surface synthesis and characterization of 9-atom wide armchair graphene nanoribbons". In: *ACS Nano* 11.2 (2017), pp. 1380–1388.

[23] K Simonov et al. "Synthesis of armchair graphene nanoribbons from the 10, 10-dibromo-9, 9-bianthracene molecules on Ag (111)". In: *Scientific Reports* 8.1 (2018), pp. 1–12.

[24] Y Fu et al. "On-Surface Synthesis of NBN-Doped Zigzag-Edged Graphene Nanoribbons". In: *Angewandte Chemie International Edition* 59.23 (2020), pp. 8873–8879.

[25] P Ruffieux et al. "On-surface synthesis of graphene nanoribbons with zigzag edge topology". In: *Nature* 531.7595 (2016), pp. 489–492.

[26] A Geim. "Graphene: status and prospects". In: *Science* 324.5934 (2009), pp. 1530–1534.

[27] A Castro Neto et al. "The electronic properties of graphene". In: *Reviews of Modern Physics* 81.1 (2009), p. 109.

[28] C Kittel. *Introduction to solid state physics*. Vol. 8. Wiley New York, 1996.

[29] P Wallace. "The band theory of graphite". In: *Physical Review* 71.9 (1947), p. 622.

[30] V Barone et al. "Electronic structure and stability of semiconducting graphene nanoribbons". In: *Nano Letters* 6.12 (2006), pp. 2748–2754.

[31] Y Chen et al. "Tuning the band gap of graphene nanoribbons synthesized from molecular precursors". In: *ACS Nano* 7.7 (2013), pp. 6123–6128.

[32] H Huang et al. "Spatially resolved electronic structures of atomically precise armchair graphene nanoribbons". In: *Scientific Reports* 2.1 (2012), pp. 1–7.

[33] R Houtsma et al. "Atomically precise graphene nanoribbons: interplay of structural and electronic properties". In: *Chemical Society Reviews* (2021).

[34] M Treier et al. "Surface-assisted cyclodehydrogenation provides a synthetic route towards easily processable and chemically tailored nanographenes". In: *Nature Chemistry* 3.1 (2011), pp. 61–67.

[35] G Whitesides et al. "Molecular self-assembly and nanochemistry: a chemical strategy for the synthesis of nanostructures". In: *Science* 254.5036 (1991), pp. 1312–1319.

[36] A Kühnle. "Self-assembly of organic molecules at metal surfaces". In: *Current Opinion in Colloid & Interface Science* 14.2 (2009), pp. 157–168.

[37] J Barth. "Molecular architectonic on metal surfaces". In: *Annu. Rev. Phys. Chem.* 58 (2007), pp. 375–407.

[38] E Arunan et al. "Definition of the hydrogen bond (IUPAC Recommendations 2011)". In: *Pure and Applied Chemistry* 83.8 (2011), pp. 1637–1641.

[39] J Ubink et al. "Bias-induced conformational switching of supramolecular networks of trimesic acid at the solid-liquid interface". In: *The Journal of Chemical Physics* 148.17 (2018), p. 174703.

[40] M Lackinger et al. "Self-assembly of Benzene- Dicarboxylic acid isomers at the liquid solid interface: steric aspects of hydrogen bonding". In: *The Journal of Physical Chemistry B* 108.36 (2004), pp. 13652–13655.

[41] M Lackinger et al. "Dynamics of Grain Boundaries in Two-Dimensional Hydrogen-Bonded Molecular Networks". In: *Small* 1.5 (2005), pp. 532–539.

[42] A Dmitriev et al. "Supramolecular assemblies of trimesic acid on a Cu (100) surface". In: *The Journal of Physical Chemistry B* 106.27 (2002), pp. 6907–6912.

[43] S Griessl et al. "Self-assembled two-dimensional molecular host-guest architectures from trimesic acid". In: *Single Molecules* 3.1 (2002), pp. 25–31.

[44] G Desiraju et al. "Definition of the halogen bond (IUPAC Recommendations 2013)". In: *Pure and Applied Chemistry* 85.8 (2013), pp. 1711–1713.

[45] T Brinck et al. "Surface electrostatic potentials of halogenated methanes as indicators of directional intermolecular interactions". In: *International Journal of Quantum Chemistry* 44.S19 (1992), pp. 57–64.

[46] P Politzer et al. "Halogen bonding and other σ-hole interactions: a perspective". In: *Physical Chemistry Chemical Physics* 15.27 (2013), pp. 11178–11189.

[47] P Politzer et al. "Chemical applications of atomic and molecular electrostatic potentials". In: (1981).

[48] J Murray et al. "Expansion of the σ-hole concept". In: *Journal of Molecular Modeling* 15.6 (2009), pp. 723–729.

[49] B Mallada et al. "Real-space imaging of anisotropic charge of σ-hole by means of Kelvin probe force microscopy". In: *Science* 374.6569 (2021), pp. 863–867.

[50] T Pham et al. "Self-assembly of pyrene derivatives on Au (111): substituent effects on intermolecular interactions". In: *Chemical Communications* 50.91 (2014), pp. 14089–14092.

[51] R Gutzler et al. "Halogen bonds as stabilizing interactions in a chiral self-assembled molecular monolayer". In: *Chemical Communications* 47.33 (2011), pp. 9453–9455.

[52] J Yoon et al. "Visualizing halogen bonds in planar supramolecular systems". In: *The Journal of Physical Chemistry C* 115.5 (2011), pp. 2297–2301.

[53] H Walch et al. "Material-and orientation-dependent reactivity for heterogeneously catalyzed carbon-bromine bond homolysis". In: *The Journal of Physical Chemistry C* 114.29 (2010), pp. 12604–12609.

[54] P Muller. "Glossary of terms used in physical organic chemistry (IUPAC Recommendations 1994)". In: *Pure and Applied Chemistry* 66.5 (1994), pp. 1077–1184.

[55] A Oyedele et al. "The growth and assembly of organic molecules and inorganic 2D materials on graphene for van der Waals heterostructures". In: *Carbon* 131 (2018), pp. 246–257.

[56] L Xu et al. "Two-dimensional self-assembled molecular structures formed by the competition of van der Waals forces and dipole–dipole interactions". In: *The Journal of Physical Chemistry C* 116.1 (2012), pp. 1061–1069.

[57] S Furukawa et al. "Structural Transformation of a Two-Dimensional Molecular Network in Response to Selective Guest Inclusion". In: *Angewandte Chemie* 119.16 (2007), pp. 2889–2892.

[58] H Gao et al. "In-plane Van der Waals interactions of molecular self-assembly monolayer". In: *Applied Physics Letters* 106.8 (2015), p. 081606.

[59] H Ascolani et al. "Van der Waals interactions in the self-assembly of 5-amino [6] helicene on Cu (100) and Au (111)". In: *Chemical Communications* 50.90 (2014), pp. 13907–13909.

[60] D Ebeling et al. "London dispersion directs on-surface self-assembly of [121] tetramantane molecules". In: *ACS Nano* 11.9 (2017), pp. 9459–9466.

[61] P Messina et al. "Direct observation of chiral metal-organic complexes assembled on a Cu (100) surface". In: *Journal of the American Chemical Society* 124.47 (2002), pp. 14000–14001.

[62] M Matena et al. "On-surface synthesis of a two-dimensional porous coordination network: Unraveling adsorbate interactions". In: *Physical Review B* 90.12 (2014), p. 125408.

[63] J Park et al. "Interchain interactions mediated by Br adsorbates in arrays of metal–organic hybrid chains on Ag (111)". In: *The Journal of Physical Chemistry C* 115.30 (2011), pp. 14834–14838.

[64] F Bebensee et al. "A surface coordination network based on copper adatom trimers". In: *Angewandte Chemie International Edition* 53.47 (2014), pp. 12955–12959.

[65] L Yan et al. "Stabilizing and Organizing Bi3Cu4 and Bi7Cu12 Nanoclusters in Two-Dimensional Metal–Organic Networks". In: *Angewandte Chemie* 130.17 (2018), pp. 4707–4711.

[66] *Introduction to Metal-Ligand Interactions*. [Online; accessed 2021-11-08]. Jan. 2020. URL: `https://chem.libretexts.org/Courses/Saint_Marys_College_Notre_Dame_IN/CHEM_342%5C%3A_Bio-inorganic_Chemistry/Assignments/Worksheets/2%5C%3A_Introduction_to_Metal-Ligand_Interactions'`.

[67] F Ullmann et al. "Ueber synthesen in der biphenylreihe". In: *Berichte der Deutschen Chemischen Gesellschaft* 34.2 (1901), pp. 2174–2185.

[68] M Lackinger. "Surface-assisted Ullmann coupling". In: *Chemical Communications* 53.56 (2017), pp. 7872–7885.

[69] R Houtsma. "On-surface synthesis of chevron-like graphene nanoribbons from a molecular precursor". MA thesis. University of Groningen, 2019.

[70] J Bjork et al. "Zipping up: cooperativity drives the synthesis of graphene nanoribbons". In: *Journal of the American Chemical Society* 133.38 (2011), pp. 14884–14887.

[71] T Wang et al. "Confined on-surface organic synthesis: Strategies and mechanisms". In: *Surface Science Reports* 74.2 (2019), pp. 97–140.

[72] F Tautz. "Structure and bonding of large aromatic molecules on noble metal surfaces: The example of PTCDA". In: *Progress in Surface Science* 82.9-12 (2007), pp. 479–520.

[73] A Narita et al. "Solution and on-surface synthesis of structurally defined graphene nanoribbons as a new family of semiconductors". In: *Chemical Science* 10.4 (2019), pp. 964–975.

[74] Z Chen et al. "Graphene nanoribbons: on-surface synthesis and integration into electronic devices". In: *Advanced Materials* 32.45 (2020), p. 2001893.

[75] X Zhou et al. "Modified Engineering of Graphene Nanoribbons Prepared via On-Surface Synthesis". In: *Advanced Materials* 32.6 (2020), p. 1905957.

[76] L Talirz et al. "Termini of bottom-up fabricated graphene nanoribbons". In: *Journal of the American Chemical Society* 135.6 (2013), pp. 2060–2063.

[77] G Binnig et al. "Scanning tunneling microscopy". In: *Surface science* 126.1-3 (1983), pp. 236–244.

[78] S Lindsay. *Introduction to nanoscience.* Oxford University Press, 2010.

[79] J Chen. *Introduction to Scanning Tunneling Microscopy Third Edition.* Oxford University Press, USA, 1993.

[80] A Dweydari et al. "Work function measurements on (100) and (110) surfaces of silver". In: *physica status solidi (a)* 27.1 (1975), pp. 223–230.

[81] Hoffman Physics Harvard. *STM: more technical details.* [Accessed September 14 2021]. URL: http://hoffman.physics.harvard.edu/research/STMtechnical.php.

[82] J Bardeen. "Tunnelling from a many-particle point of view". In: *Physical Review Letters* 6.2 (1961), p. 57.

[83] J Tersoff et al. "Theory and application for the scanning tunneling microscope". In: *Physical Review Letters* 50.25 (1983), p. 1998.

[84] J Tersoff et al. "Tip-dependent corrugation of graphite in scanning tunneling microscopy". In: *Physical Review Letters* 65.9 (1990), p. 1132.

[85] J Chen. "Effects of m$\neq$ 0 tip states in scanning tunneling microscopy: the explanations of corrugation reversal". In: *Physical Review Letters* 69.11 (1992), p. 1656.

[86] I Giaever et al. "Study of superconductors by electron tunneling". In: *Physical Review* 122.4 (1961), p. 1101.

[87] R Feenstra et al. "Real-space determination of surface structure by scanning tunneling microscopy". In: *Physica Scripta* 1987.T19A (1987), p. 55.

[88] R Feenstra et al. "Tunneling spectroscopy of the Si (111) 2$\times$ 1 surface". In: *Surface Science* 181.1-2 (1987), pp. 295–306.

[89] K Oura et al. *Surface science: an introduction.* Springer Science & Business Media, 2013.

[90] Wikimedia Foundation Inc. *Low-energy electron diffraction — Wikipedia, The Free Encyclopedia.* [Online; accessed 07-January-2022]. 2022. URL: https://en.wikipedia.org/w/index.php?title=Low-energy_electron_diffraction&oldid=1057048641.

[91] I Horcas et al. "WSXM: A software for scanning probe microscopy and a tool for nanotechnology". In: *Review of Scientific Instruments* 78.1 (2007), p. 013705.

[92] R Behrisch et al. *Sputtering by particle bombardment.* Vol. 1. Springer-Verlag Berlin, 1981.

[93] A van Bondi. "van der Waals volumes and radii". In: *The Journal of Physical Chemistry* 68.3 (1964), pp. 441–451.

[94] I Píš et al. "Surface-confined polymerization of halogenated polyacenes: the case of dibromotetracene on Ag (110)". In: *The Journal of Physical Chemistry C* 120.9 (2016), pp. 4909–4918.

[95] W Wang et al. "Single-molecule resolution of an organometallic intermediate in a surface-supported Ullmann coupling reaction". In: *Journal of the American Chemical Society* 133.34 (2011), pp. 13264–13267.

[96] Q Fan et al. "Surface-assisted formation, assembly, and dynamics of planar organometallic macrocycles and zigzag shaped polymer chains with C–Cu–C bonds". In: *Acs Nano* 8.1 (2014), pp. 709–718.

[97] K Chung et al. "Electronic structures of one-dimensional metal–molecule hybrid chains studied using scanning tunneling microscopy and density functional theory". In: *Physical Chemistry Chemical Physics* 14.20 (2012), pp. 7304–7308.

[98] Q Fan et al. "Surface adatom mediated structural transformation in bromoarene monolayers: precursor phases in surface Ullmann reaction". In: *ACS Nano* 12.3 (2018), pp. 2267–2274.

[99] Z Zeng et al. "Chemisorption-Induced Formation of Biphenylene Dimer on Ag (111)". In: *Journal of the American Chemical Society* (2021).

[100] L Feng et al. "On-surface synthesis of planar acenes via regioselective aryl–aryl coupling". In: *Chemical Communications* 56.36 (2020), pp. 4890–4893.

[101] H Zhang et al. "On-surface synthesis of rylene-type graphene nanoribbons". In: *Journal of the American Chemical Society* 137.12 (2015), pp. 4022–4025.

[102] K Sun et al. "Substrate-controlled synthesis of 5-armchair graphene nanoribbons". In: *The Journal of Physical Chemistry C* 124.21 (2020), pp. 11422–11427.

7 Acknowledgements

This endeavor would not have been possible without the guidance and help of the Surface Science group. Therefore, I want to express my gratitude to all who have helped me during my master project.

First of all, I would like to thank prof. dr. Meike Stöhr for giving me the opportunity to do this exciting project. Dear Meike, already in my bachelor Applied Physics I became interested in surface science by your lectures, which resulted in me doing my bachelor project with you. A small bite of surface science left me lingering for more. When Koen mentioned a project involving LT during a lab tour, I did not hesitate to email you about this master project. Thank you for the guidance and insightful discussions which helped me gain a better understanding of the project and surface science in general.

I would like to thank prof. dr Tamalika Banerjee for agreeing to be my second examiner and her consideration in grading my work. Thank you for your questions after my presentation, which forced me to critically think about the implications of my project.

My special gratitude goes out to Koen Houtsma, my daily supervisor. Dear Koen, thank you for teaching me how to use the STM and your supervision. I appreciated your patience and you knew how to answer my every question. Your knowledge on the subject helped me tremendously during the project and made me never hesitate to ask you when I did not understand something. Your endless enthusiasm sparked motivation in me.

I would also like to thank Miki for her technical support in the lab. Dear Miki, thank you for your kind words which gave me confidence during my project, both in and outside the lab.

Furthermore, I would like to thank all members of the Surface Science group, Meike, Miki, Koen, Baoxin, Wenbo, Joris, Qiankun and Adam for the nice working environment and all the fun we had.

Lastly, I would like to thank Lars Bokkers for the food for thought.

A Investigated samples

<p style="text-align:center">Table 2: Overview of all samples investigated.</p>

Sample	Coverage (A)	Deposition rate (A/min)	Deposition temperature (C)	Post-deposition annealing temperature (C)	Description
1a	1.06	0.28	RT		Chevron network, homochiral network, heterochiral chains
1b				89.3	Networks of heterochiral chains
1c				201	Molecules clumped together
1d				300.4	Molecules clumped together
2a	1.37	0.39	100.6		Networks of heterochiral chains
2b				158	Shorter heterochiral chains
2c				199.5	Molecules clumped together
2d				256.7	Molecules clumped together
3a	1.44	0.21	120.2		Large networks of heterochiral chains
3b				133.8	Large networks of heterochiral chains
3c				151.3	Shorter heterochiral chains
4a	1.05	0.28	31.1		Chevron network, heterochiral chains
5a	1.59	0.27	33.5		Chevron network, heterochiral chains
5b				149.6	Networks of heterochiral chains, heterochiral chains
5c				159.7	Molecules clumped together, occasionally heterochiral chains
5d				172.1	Molecules clumped together, occasianally heterochiral chains
6a	1.46	0.37	151		Low coverage, networks of heterochiral chains
6b				179.6	Molecules clumped together
7a	1.7	0.69	150.7		Large networks of heterochiral chains
8a	1.9	0.20	120.6		No measurements
8b				134.8	Large networks of heterochiral chains
9a					Bare Ag(111) surface
10a	1.16	0.29	25		Chevron, chains, 2D network of chains

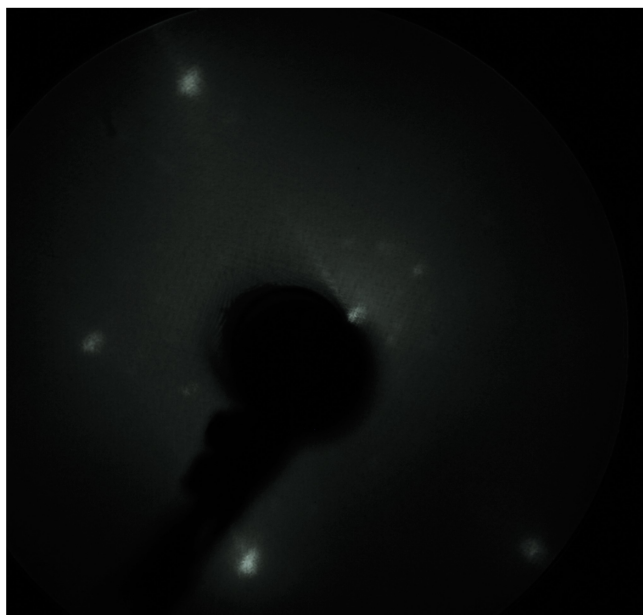# B LEED

Figure 31: The LEED-pattern showing the surface spots taken at an electron energy of 100.4eV. The (0,0)-spot is slightly to the right of the electron gun. The pattern is similar to the expected pattern of the Ag(111) surface.